In: H Cerjak (ed.): Mathematical Modelling of Weld Phenomena 3,The Institute of Materials, London 1996

TIG and Plasma Arc Modelling: a survey

J. Wendelstorf[1], I. Decker[1], H. Wohlfahrt[1]
and
G. Simon[2]

Institut für Schweißtechnik[1]
and Institut für Theoretische Physik[2],
Technische Universität Braunschweig,
Postfach 3329, D-38023 Braunschweig, Germany

Abstract

For the numerical analysis of tungsten-inert-gas-welding (GTAW or TIG) and plasma-arc-welding (PAW) processes, detailed information on both, the distribution of energy flow and excess pressure at the weld pool surface is needed. Numerical arc modelling can deliver such information, which can be used as input data for weld pool modelling or for the optimization of arc- and torch-parameters, as well as demonstrating physical arc behaviour.

The state-of-the-art in modelling of DCEN-gas-tungsten-arcs is reviewed. By application of justified two-dimensional radial symmetric arc models, computation of the arc should include all significant electric, diffusive and convective transport mechanisms. Even cathode phenomena, anode evaporation and turbulence has been included. The results can be compared with arc temperature measurements. Therefore, including boundary layer phenomena at the anode and cathode, quantitative computations are possible without fitting arc parameters to experimental data (*ab initio modelling*).

Future directions of research, like further model integration and three dimensional arc models for the simulation of high-speed welding arcs are proposed.

Contents

1 Introduction

Understanding and modelling of electric arcs is a matter of scientific interest since the first detection of the arcing phenomena itself 150 years ago. The electric arc is applied for welding since the 1930's and first plasma torches where introduced in the 1950's. The technology is based on experimental experience rather than theoretical understanding and prediction. Nevertheless, significant progress has been made in *ab initio* computation of arc phenomena by the indroduction of two-dimensional numerical methods in 1977.

A fundamental introduction into arc physics including a comprehensive survey of the earlier works was given by Maecker in 1956 [MF57]. The outstanding review of electric arc applications given by Pfender in 1978 [Pfe78] and Guile in 1984 [Gui84] was recently accompanied by Jönsons article [JSCQ94], covering the numerical model development in the last decades.
This paper is dedicated to summarize the theoretical basis of TIG-arc[1] modelling and its extensions to the plasma arc, thus discussing the scientific foundation of model utilisation for industrial and laboratory applications.

1.1 Scope of arc modelling for welding applications

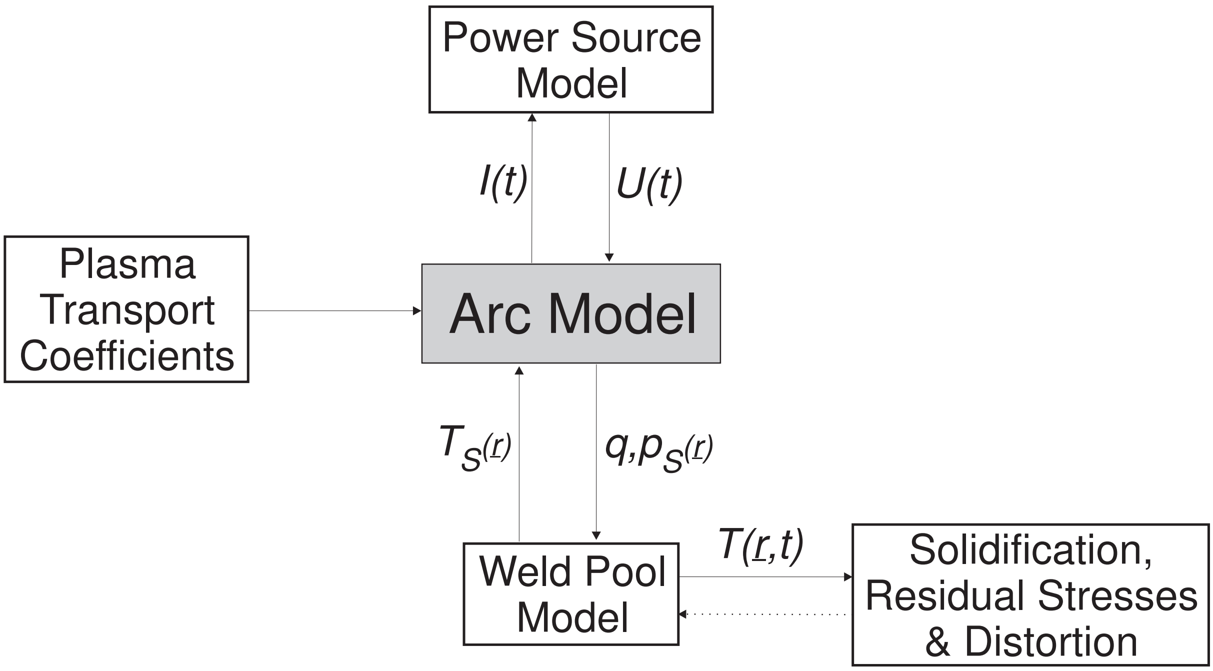

Figure 1: The arc modelling module within the overal welding process simulation.

Modelling of electric arcs includes a wide range of physical phenomena of high complexity. Additionally, for materials processing applications like welding, computation of arc properties is only one task within the simulation of the overall welding procedure (see figure 1).
The interfaces to models of the molten pool are of special importance. Regardless the parabolic (downstream) nature of the DCEN arc, there are important influences of the workpiece (anode) on arc characteristics and behaviour. These interaction takes place by weld pool depression (changing the anode geometry) and due to metal evaporation *feeding* the arc with low ionization potential material and thus locally increasing electrical conductivity. From welding practice, important effects of anode surface inhomogenities were also reported.

[1]This paper deals only with DCEN TIG- and Plasma-arcs, i.e. DC-arcs struck between a negative polarity tungsten electrode and a metal anode (workpiece) – for other welding arcs, quantitative *ab initio* models are not known.

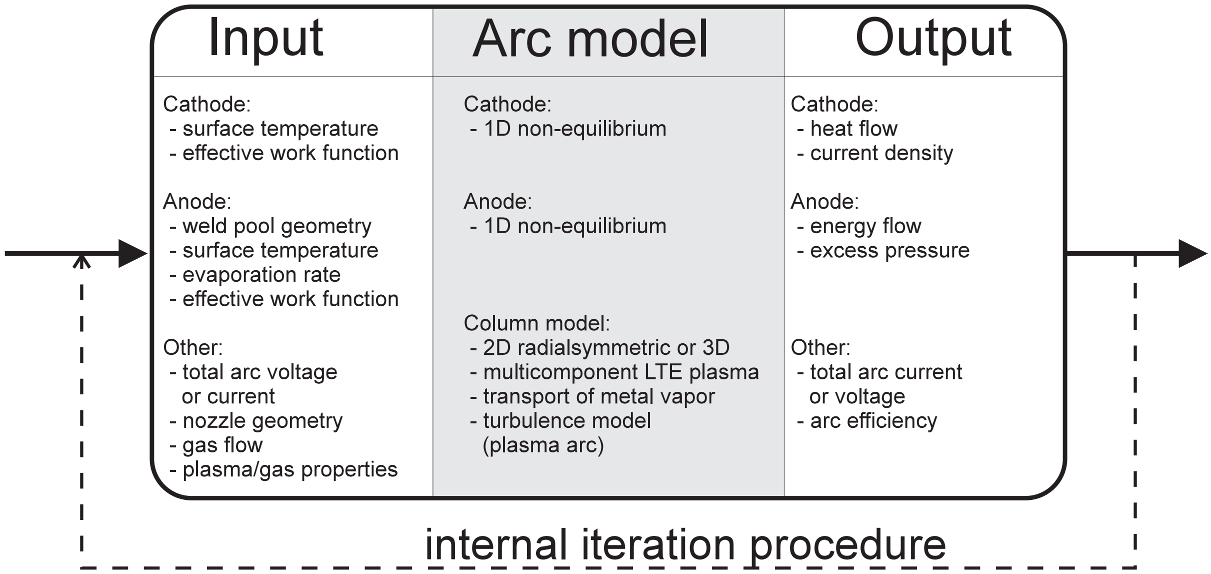

Figure 2: Definition of an arc modelling module.

For keeping things modular, one can define an arc model as a *black box* (see figure 2). The most important result for welding applications is the energy distribution supplied to the workpiece by the arc. Especially for plasma arc welding, the anodic excess pressure distribution also becomes important for deep penetration effects by the formation of a vapor capillary (*keyhole*). For quantitative calculations, process parameter studies and optimizations, all physical processes significantly influencing to this target functions have to be taken into account. Since the complexity can not be accurately handeled up to now, evaluation of such models should include a critical look at the role of *hidden parameters* widely used for fitting results to measured arc temperature distributions, e.g. a prescribed cathodic current density distribution.

1.2 Fundamental welding arc physics

As sketched in figure 3, the arc consists of a thermal plasma surrounded by electrode layers, where a major part of the voltage drop is located and the conditions of local thermodynamic equilibrium (LTE) are not applicable. These anode- and cathode *falls* are thin sheaths around the active electrode regions, thus forming the interface between the hot plasma and the comparatively cold electrodes. In most cases, one dimensional treatment of these layers is justified, while the main arc core (arc column) has to be treaten two dimensional (assuming cylindrical symmetry), or even three dimensional for high speed welding applications and non perpendicular incidence of the arc.
The arc column can be treated as a conducting fluid with locally identical species temperatures, or by a two fluid model, taking differences between the electron and heavy particles temperature into account.
While most published arc models are in fact arc column models, self consistent boundary conditions can be computed only by including the non-LTE-layers. This is especially important at the cathode, because the arc column is very sensitive to cathode processes [Wes89].

The nonlinearities are in general very important. Conductivities and other transport coefficents in the arc plasma vary by several orders of magnitude. Thus, omitting some physical detail can lead to totally different energy distributions supplied to the workpiece – the most important result the model should deliver – while the arc temperature distribution in the arc core is still in reasonable agreement with the measured one.
It was recently shown, that the development of an integrated arc simulation as sketched in figure 2 is possible, but there is a number of important limitations in the current model [ZLMH95]. As an example, accurate and self-consistent computation of the anode and cathode potential drop may be regarded as an unsolved problem.

1.3 Outline of the paper

This review is an attempt to form a starting point for future attempts on TIG and plasma arc modelling for welding applications. For this reason, the equations needed for a quantitative description of the arc column are summarized in section 2. Transport coefficients are briefly characterized (2.2), a starting point for turbulence modelling is proposed (2.3) and the numerical methods are mentioned (2.4).
Proper treatment of the electrode regions (section 3) is crucial for quantitative modelling, but still under development. A model is proposed (3.1), which may form the basis for future cathode and anode fall treatments. Results for a typical cathode boundary layer are presented (3.1.5 and the consideration of the anode fall region is briefly discussed (3.2).
The open literature results presented in section 4, for free burning argon arcs, and in section 5, for constricted plasma arcs, should deliver an impression on benefits and constraints actually coming out of this research area.
In the last section 6, our personal view on the knowledge actually available to the public and its scientific and industrial implications is summarized.
References are given in alphabetic order and a glossary of symbols can be found in 6.3.

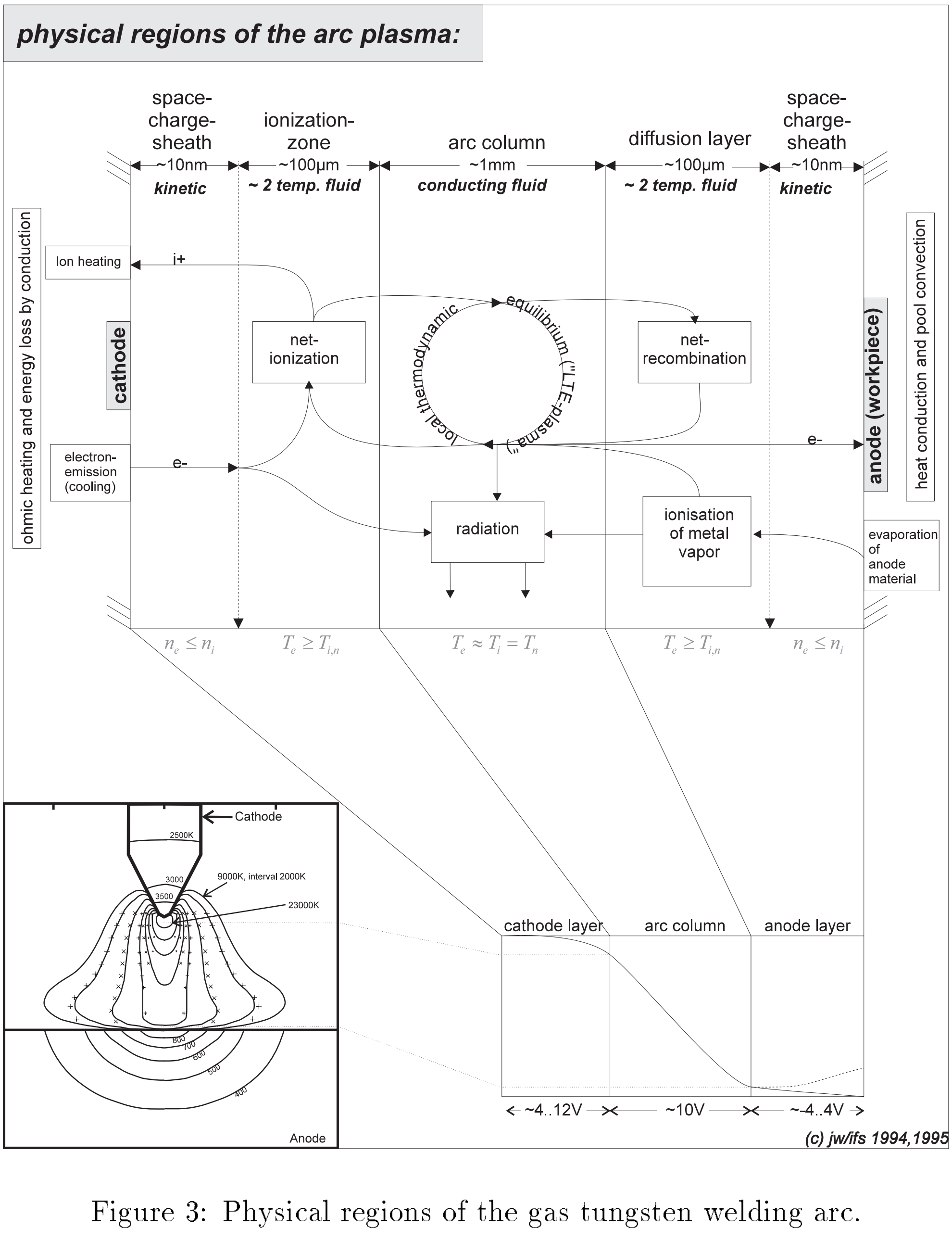

Figure 3: Physical regions of the gas tungsten welding arc.

2 Theory of the arc column

Beside the electrode layers, the arc consists of a *thermal plasma.* For practical welding applications its radial extension is about 0.5–5mm and it is filling the overall electrode gap (*arc length*) of about 0.5–5mm.
This column plasma mainly consists of ionized inert shielding gas (Ar, He) and some ionized metal vapor near the anode. Beside cathode erosion studies [ZHP94], cathode evaporation becomes of primary importance only for DCEP- or AC-arc operation or non-tungsten cathodes, all of them not considered here.
For modelling the arc column plasma, a number of basic assumptions is well justified and accepted:

- The fluid flow in the column of a TIG-arc is laminar (Re < 400).
- The fluid flow at the arc fringes and of some plasma arcs can become turbulent.
- The arc column is in local thermodynamic equilibrium (LTE), i.e. locally determined by the thermodynamic variables velocity $\vec{\mathbf{v}}$, temperature T, pressure p and enthalpy h and the electromagnetic quantities current density $\vec{\mathbf{j}}$, electric potential Φ and magnetic field $\vec{\mathbf{B}}$. This is called one-fluid ($T_e \equiv T_{i,a} =: T(\vec{\mathbf{r}})$) or two-fluid ($T_e(\vec{\mathbf{r}}) \neq T_{i,a} \equiv T_h(\vec{\mathbf{r}})$) hydrodynamic treatment.
- The arc column plasma is quasi-neutral, i.e. free of space charges.
- The arc column can be treated two-dimensional, assuming cylindrical symmetry, but one-dimensional models fail because of strong inhomogenities in both radial and axial directions.

The governing equations of the arc column are deducted from magnetohydrodynamics (MHD) and general fluid dymamics [ADDG92, Pan93, BSL60].

2.1 Mathematical model

2.1.1 Mass continuity

First, the equation of mass continuity (written in the *conservation form*)

$$\frac{\partial}{\partial t}\rho + \vec{\nabla} \cdot (\rho \vec{\mathbf{v}}) = 0, \tag{1}$$

has to be fullfilled. For small Mach-numbers (Ma$= |\vec{\mathbf{v}}|/v_c < 0.3$, i.e. the flow speed is well below the local speed of sound [Pan93, p.415]), the plasma fluid can be regarded as *incompressible*

$$\vec{\nabla} \cdot \vec{\mathbf{v}} = 0 \quad , \quad \rho \approx \text{const} \ , \tag{2}$$

an assumption actually used by all authors.

2.1.2 Momentum balance

From Newtons second law, the momentum equation is derived ([Pan93, p.414] and [BSL60, p.76]):

$$\underbrace{\rho\frac{D}{Dt}\vec{\mathbf{v}}}_{\substack{\text{momentum change per}\\\text{time interval and}\\\text{convection loss per}\\\text{volume}}} = \underbrace{-\vec{\nabla}p}_{\substack{\text{force of the scalar}\\\text{pressure per}\\\text{volume}}} \underbrace{+\vec{\nabla}\cdot\left(\mu\underline{\underline{\pi}}\right)}_{\substack{\text{friction loss per}\\\text{volume}}} \underbrace{+\vec{\mathbf{j}}\times\vec{\mathbf{B}}}_{\substack{\text{Lorenz-force per}\\\text{volume}}} \tag{3}$$

The strain-rate tensor $\underline{\underline{\pi}}$ is defined as usual [BSL60, p.88]. The Froude Number[2] of arc plasmas is about 10^6, thus gravity can be neglected. Natural convection forces can be neglected in the arc plasma, but become important for gas shielding effects of the workpiece, e.g. argon is heavier than the surrounding atmosphere and helium is much lighter.

2.1.3 Energy balance

The compression work $\vec{\mathbf{v}}\cdot\vec{\nabla}p$ and viscous dissipation $\vec{\mathbf{v}}:\underline{\underline{\pi}}$ can be neglected, because the Mach-Number is about 0.1 and Prandtl-Numbers[3] Pr= $c_p\mu/\lambda$ are small $(0.03\ldots0.7)$. Thus energy balance in terms of plasma enthalpy h reads

$$\underbrace{\rho\frac{D}{Dt}h}_{\substack{\text{enthalpy change and}\\\text{convection loss per unit}\\\text{volume}}} = \underbrace{\vec{\nabla}\cdot\vec{\mathbf{q}}}_{\text{heat flux}} \underbrace{+\vec{\mathbf{j}}\cdot\vec{\mathbf{E}}}_{\substack{\text{Joule}\\\text{heating}}} \underbrace{-S_R}_{\substack{\text{radiation}\\\text{loss}}} \tag{4}$$

The heat flux is given by conduction, enthalpy transport by the (current carrying) electrons and the diffusion–thermo (Dufuor) effect from the diffusion of metal vapor into the shielding gas plasma:

$$\vec{\mathbf{q}} = \frac{\lambda}{c_p}\vec{\nabla}h + \frac{5k_B}{2e}\frac{\vec{\mathbf{j}}}{c_p}h + \vec{\nabla}\cdot\left[\sum_i\left(\rho D - \frac{\lambda}{c_p}\right)(h_i)\vec{\nabla}C_i\right]. \tag{5}$$

Typical for thermal plasmas is the phenomenon of temperature split at pressures below 0.1 MPa, at temperatures below 9000K and near the electrodes. The electrons became decoupled from the heavy particles – they must be treated as seperate fluid. For this reason, accurate modelling requires the electrons and the heavy particles to be treaten as different fluids (two-fluid model). The energy balance of the electrons becomes

$$\rho_e\frac{D}{Dt}h_e = \vec{\nabla}\cdot\vec{\mathbf{q_e}} + \vec{\mathbf{j}}\cdot\vec{\mathbf{E}} - S_R - \dot{E}_{eh} \tag{6}$$

[2]inertia force/gravity force

[3]describing the relation of momentum diffusity to thermal diffusity [And90, p.67].

with the electron heat flux

$$\vec{\mathbf{q_e}} = \frac{\lambda}{c_p} \vec{\nabla}\, h_e + \frac{5k_B}{2e} \frac{\vec{\mathbf{j}}}{c_p}\, h_e \tag{7}$$

and the energy exchange term

$$\dot{E}_{eh} = \sum_s \frac{2m_e}{m_s} \cdot {}^3\!/_2\, k_B\ (T_e - T_h)\, n_e\, n_s v_e^{th}\, Q_{es} \tag{8}$$

Analogous, neglecting transport of ionization energy [Kru70], the enthalpy balance of the heavy particles becomes

$$\rho \frac{D}{Dt} h_h = \vec{\nabla} \cdot \vec{\mathbf{q_h}} + \dot{E}_{eh} \tag{9}$$

with the heavy particles heat flux

$$\vec{\mathbf{q_h}} = \frac{\lambda_s}{c_p} \vec{\nabla}\, h_h + \vec{\nabla} \cdot \left[\sum_i \left(\rho D - \frac{\lambda}{c_p} \right) (h_i)\, \vec{\nabla}\, C_i \right].$$

The heat conductivity is given by its individual species contributions and the reaction term ($\lambda_h = \lambda_a + \lambda_i + \lambda_r$).

2.1.4 Transport of metal vapor

In the case of arc welding, the anode (workpiece) can be heated up to evaporation temperature. For this reason, additionally one has to solve a diffusion equation for the metal vapor into the shielding gas plasma:

$$\rho\ \frac{D}{Dt} C_i = \vec{\nabla} \cdot \left[D\, \vec{\nabla}\ (\rho C_i) \right] \tag{10}$$

2.1.5 Maxwell's equations

Regardless the importance of hydrodynamic transport phenomena, the arc is mainly an electrical phenomenon. Taking into account the column plasma is electrically neutral (quasineutrality, $\rho_{el} \approx 0$), the generalized Ohm's law becomes [Vil82]

$$\vec{\mathbf{j}} = \sigma \cdot \left\{ \vec{\mathbf{E}} + \vec{\mathbf{v}} \times \vec{\mathbf{B}} - \frac{1}{n_e e} \vec{\mathbf{j}} \times \vec{\mathbf{B}} + 0.41 \cdot \frac{k_\mathrm{b}}{2e} \vec{\nabla} T \right\}, \tag{11}$$

The current is driven mainly by the electric field ($\vec{\mathbf{v}} \times \vec{\mathbf{B}} \ll \vec{\mathbf{E}}$) and the Hall-current can be neglected Most authors also neglect thermo-diffusion, using the rather questionable simplification $\vec{\mathbf{j}} = \sigma \vec{\mathbf{E}}$. Thus, current continuity

$$\nabla \cdot \vec{\mathbf{j}} = 0 \tag{12}$$

gives a poisson-type equation

$$\vec{\nabla} \cdot \left(\sigma \vec{\nabla}\, \Phi \right) = 0.$$

for the electric potential Φ. Using $\nabla \cdot \vec{\mathbf{B}} = 0$, after introduction of the vector potential $\vec{\mathbf{B}} = \vec{\nabla} \times\ \vec{\mathbf{A}}$, from Maxwell's equations

$$\vec{\nabla} \times\ \vec{\mathbf{H}} = \vec{\mathbf{j}} + \dot{\vec{\mathbf{B}}} \quad , \quad \vec{\mathbf{B}} = \mu_o \mu_r \vec{\mathbf{H}} \quad , \quad \mu_r \simeq 1,$$

the vector potential (and thus the magnetic field produced by the arc) can be computed from the current densities by Ampere's law:

$$\vec{\nabla} \times \vec{\mathbf{B}} = \triangle \vec{\mathbf{A}} = -\mu_o \vec{\mathbf{j}} \quad , \quad \vec{\nabla} \cdot \vec{\mathbf{A}} = 0 \tag{13}$$

For the the radial-symmetric case, the magnetic field is simply given by

$$B_\theta = \frac{\mu_o}{r} \int_0^r j_z \xi d\xi,$$

or alternatively by solving the magnetic diffusion equation [MS86]

$$\frac{\partial}{\partial z}\left(\frac{1}{\sigma}\frac{\partial B_\theta}{\partial z}\right) + \frac{\partial}{\partial r}\left(\frac{1}{r\sigma}\frac{\partial (rB_\theta)}{\partial r}\right) = 0$$

and computing current density from

$$\mu_o j_z = \frac{1}{r}\frac{\partial}{\partial r}(rB_\theta) \text{ and } \mu_o j_r = -\frac{\partial B_\theta}{\partial z}.$$

2.1.6 Saha's equation and equation-of-state

For determination of the plasma composition ($n_{e,i,a}$), Saha's equation describing ionization equilibrium and the (ideal gas) equation of state is used to close the system. In the most general case of different electron temperature T_e and heavy particles temperature T_h, Saha's equation becomes [Pot66]:

$$n_e \left(\frac{n_r}{n_{r-1}}\right)^{T_h/T_e} = \frac{2\,g_r}{g_{r-1}} \left(\frac{m_e\,k_\mathrm{b}\,T_e}{2\,\pi\,\hbar^2}\right)^{3/2} \exp\left(-\frac{E_r - \delta E_r}{k_\mathrm{b} T_e}\right) \quad , \tag{14}$$

with the lowering of the ionization energy

$$\delta E_r = \frac{re^2}{4\pi\epsilon_o \lambda_\mathrm{Debye}}. \tag{15}$$

g_r and g_{r-1} denote the partition functions of the ions ($r = 1, \ldots$) and neutral atoms ($r = 0$), respectively [DF65]. The Debye shielding length follows from

$$\lambda_\mathrm{Debye} = \left\{\frac{e^2}{\epsilon_o k_\mathrm{b}} \sum_\alpha \frac{Z_\alpha^2 n_\alpha}{T_\alpha}\right\}^{-1/2} \tag{16}$$

Using quasi-neutrality $n_e = \sum_{a,Z} Z\, n_Z^a$ and Dalton's law

$$\begin{aligned} p &= n_e k_\mathrm{b} T_e + \sum_\alpha n_\alpha k_\mathrm{b} T_\alpha \\ &= \rho\, R\, T_e \left(\frac{n_e}{n_e + n_a} + \frac{T_h}{T_e}\right), \end{aligned}$$

electron density can be computed. For accurate computations of high density plasmas, one may include the Debye term

$$p_\text{Debye correction} = -\frac{e^2 n_e}{12\pi\epsilon_o \lambda_\mathrm{Debye}}.$$

2.1.7 Remarks

For the 2-D case, metal vapor effects were first implemented by Zhao et.al. [ZDE90], while most groups neglect such effects. Earlier models omitted the enthalpy formulation and decribed the column in terms of the plasma temperature T [KC86], thus getting numerical schemes not conserving the energy flow.
The 2-temperature arc column model was realized by Pfender's group [CP81, Hsu82, HP83b] in the 2-D case, while the general case of metal vapour diffusion *and* different electron and heavy particle temperatures remains untreated. Occassionally, one has to distinguish between the general (3D) formulation given above, the (published) 2-D equations and the equations really treated by the individual computer code.
A more rigorous treatment of thermal plasmas is known from other application areas (e.g. [Ben93, LOS92]), taking into account the general case of deviations from complete LTE (ASDF approach), but actually not applied to the electric arcs considered here.

2.2 Transport coefficients

The arc plasma is very sensitive to gas impurities and metal vapor. These effects are determined by the drastic variation of the transport coefficients with plasma temperature and their sensitivity to impurities [HFKC86].

2.2.1 Plasma density and enthalpy

The plasma density

$$\rho = n_e m_e + \sum_{\xi=\alpha,a} n_\xi m_\xi$$

and enthalpy $h = h_{\text{translational}} + h_{\text{excitational}} + h_{\text{chemical}}$, where

$$\begin{aligned}
h_{\text{tr}} &= 1/\rho \left[{}^5\!/_2\, k_{\text{b}} \left(n_e T_e + \sum_{\xi=\alpha,a} n_\xi T_\xi \right) \right] \\
h_{\text{ex}} &= 1/\rho \left[k_{\text{b}} \sum_{\xi=\alpha,a} T_\xi^2 n_\xi \frac{\partial \ln Z_\xi}{\partial T_\xi} \right] \\
h_{\text{ch}} &= 1/\rho \sum_\alpha n_\alpha \left(\sum_{j=1}^{\alpha} E_j - \delta E_j \right) \qquad (17)
\end{aligned}$$

are computed from plasma composition. Specific heat is computed from enthalpy by

$$c_p = \left. \frac{\partial h}{\partial T} \right|_p \simeq \frac{5 k_{\text{b}}}{2 m_h} (1 + \alpha_{ion}), \qquad (18)$$

where α_{ion} is the degree of ionization.

2.2.2 Electrical conductivity

A detailed discussion of the measurements and computations of the electrical conductivity of the plasma was given recently [DE90]. For a pure argon plasma, Devoto's fit-formula

$$\begin{aligned}
\sigma[\text{S/m}] &= 2.26 \cdot 10^6 \exp(-6.21 \cdot 10^4 / T[\text{K}]) && T < 8000\text{K} \\
&= 1.96 \cdot 10^5 \exp(-4.26 \cdot 10^4 / T[\text{K}]) && 8000\text{K} < T < 15000\text{K}
\end{aligned}$$

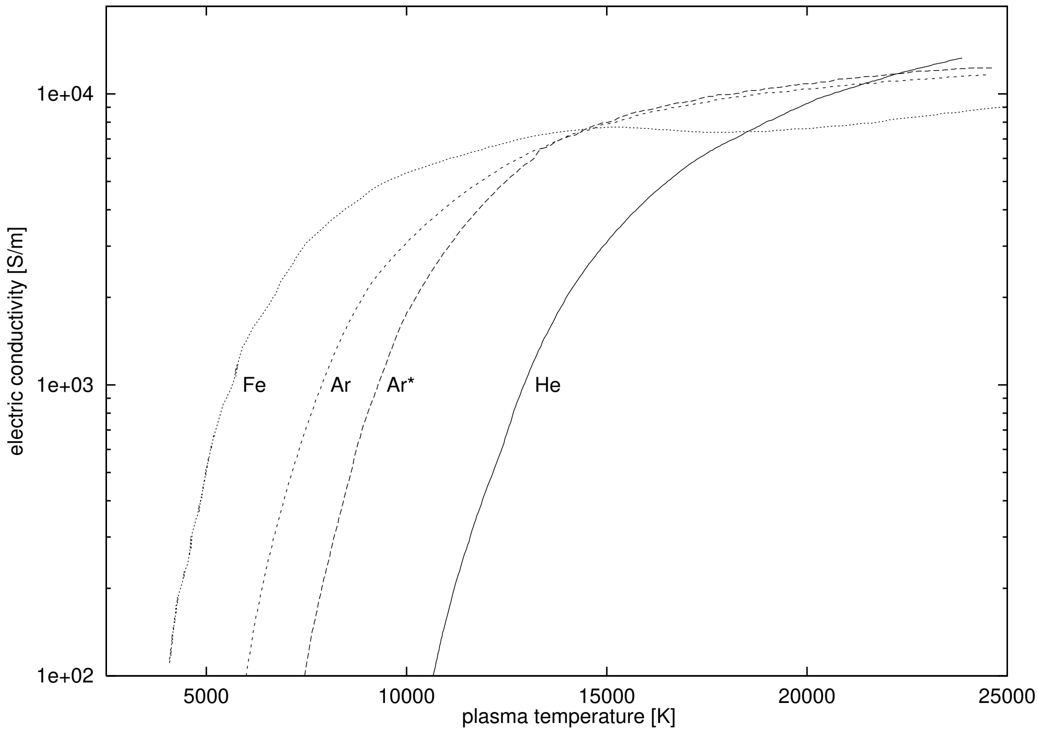

Figure 4: Temperature dependence of the electrical conductivity for pure iron [GG93], argon ($T_e/T_h = 1$ and 2^*) [HP83b] and helium [DE90] plasmas at atmospheric pressure.

can be used [Dev67a, Dev67b], while metal vapor increase and helium additions decrease electric conductivity by orders of magnitude (e.g. [Gli80] and figure 4). Obviously, the electric conductivity can be computed with acceptable accuracy.

2.2.3 Plasma heat conductivity

For a discussion of plasma heat conductivity, refer again to the work of Dunn and Eagar [DE90]. For a discussion of the temperature-split effect see Hsu's work [Hsu82, HP83b]. Especially helium give a strong increase in heat conductivity (figure 5). Accuracy due to the available cross section data seems to be sufficient.

2.2.4 Plasma viscosity

A simple fit formula for plasma viscosity was provided by [YA77], the effect of different electron- and heavy-partivles temperature is again computed by Hsu (figure 6). There are still discrepancies between the different authors and the effect of iron or aluminium vapor additions to an argon plasma is actually not published.

2.2.5 Plasma radiation

For argon plasmas, as a starting point, the fit formula of the Evans and Tankin data [ET67, MA69]:

$$S_R[\mathrm{W/m^3}] = 5600 \cdot (T[\mathrm{K}] - 9500) + 181 \cdot (T - 9500[\mathrm{K}])^2$$

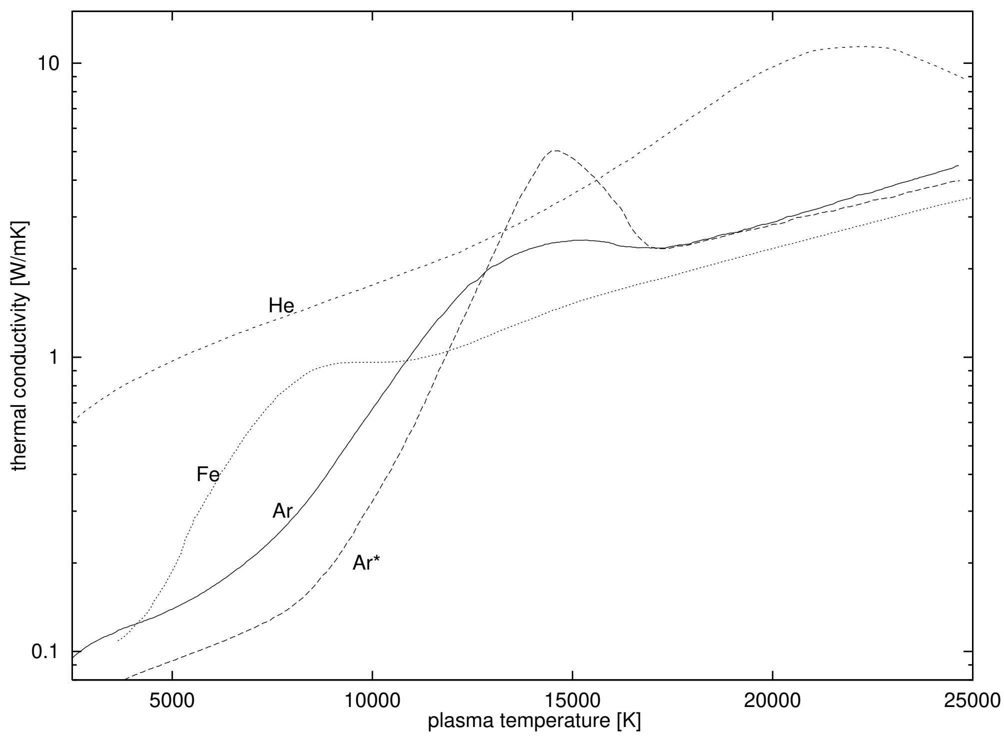

Figure 5: Temperature dependence of the plasma heat conductivity for pure iron [AIA91], argon ($T_e/T_h = 1$ and 2^*) [HP83b] and helium [DE90] plasmas at atmospheric pressure.

may be used, while metal vapor additions are increasing radiation losses by orders of magnitude (see figure 7). The radiation emission coefficient of helium were not found in open literature. Recent measurements show rapidly decreasing radiative power, when adding helium to an argon arc. In argon rich arcs, a significant proportion of the total radiative power consists of infrared radiation. In helium arcs this contribution is negligible [ZH94]. In general, calculations of the radiation emission coefficient critically depend on the *optical thin plasma* assumption.

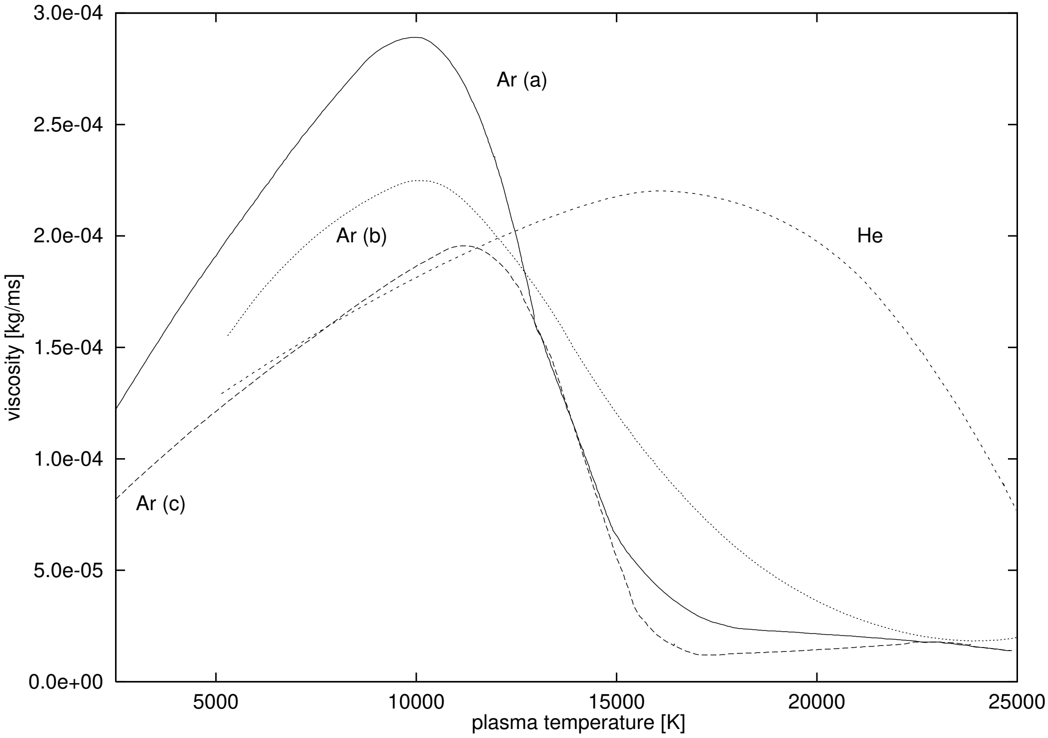

Figure 6: Temperature dependence of the viscosity for argon ((a):$T_e/T_h = 1$ and c:2, [HP83b] and (b):[MM73]) and helium [MM73] plasmas at atmospheric pressure.

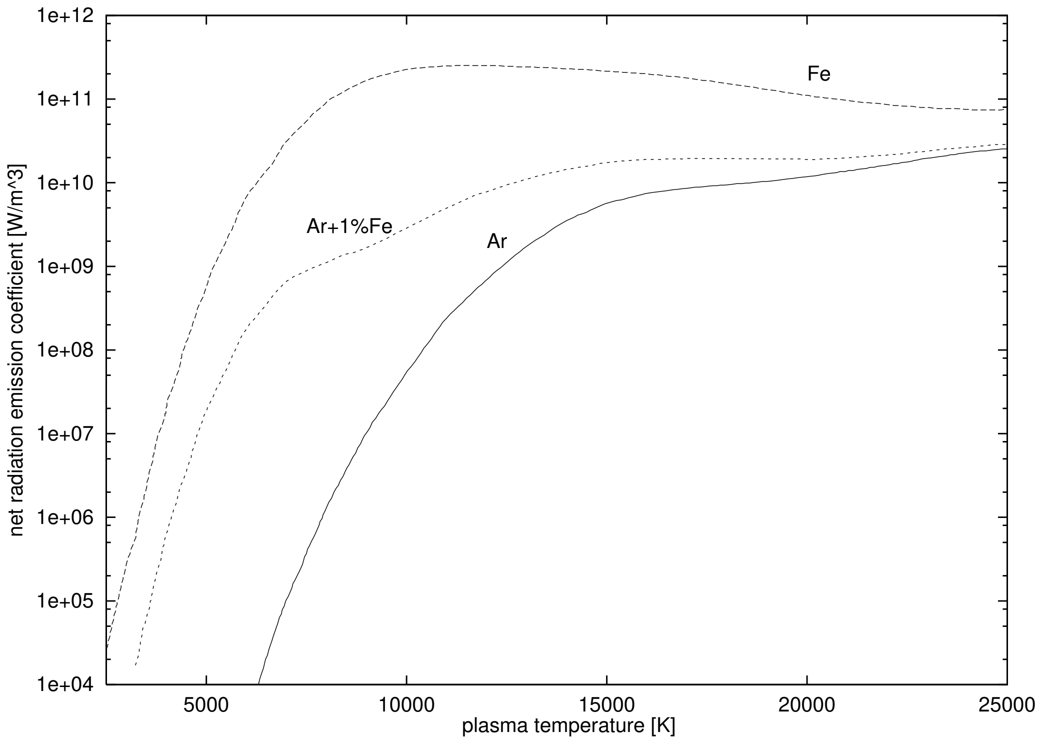

Figure 7: Temperature dependence of the net radiation emission coefficient for pure argon [EPB90], iron and argon + 1% iron [GG93] plasmas at atmospheric pressure.

2.3 Turbulence modelling

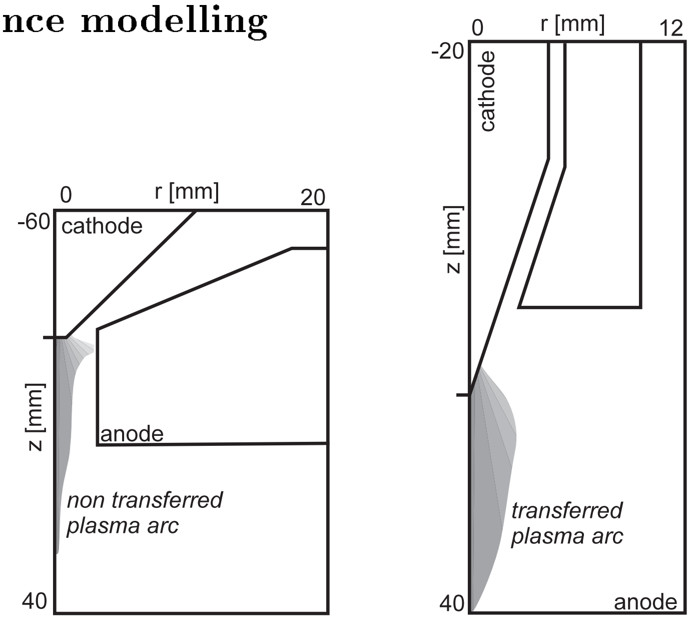

Figure 8: Plasma arc configurations [MK93, CDR+93].

Conventional TIG-arcs are *free-burning*, i.e. the cathode jet is dominated by the magnetohydrodynamic pumping from the arc itself but not by the gas flow from the nozzle. The Reynolds number is less than 500, the flow is laminar. In the plasma arc welding process (figure 8), the plasma gas flow is constricted by a metallic nozzle around the cathode. Such arcs show Reynolds numbers well above 1000 – the flow may become turbulent.
Turbulence is almost impossible to predict, i.e. it is not predictable in the sence of macroscopic modelling. However it seems that computer simulations of such fluids will allow engineers to evaluate their torch design. Not the turbulence itself, but the mean flow may be described by models of the K-ϵ-type [LS72, MP94].Based on the fundamentals developed in the seventies [Han70, Rod72, LS74b], the turbulence model sketched below was recently applied for a plasma arc calculation [MK93].
The K-ϵ-turbulence model is formulated by replacing viscosity μ with its mean value $\mu_{\text{eff}} = \mu_l + \mu_t$, heat conductivity $\lambda_{\text{eff}} = \lambda_l + \lambda_t$ and diffusion coefficient $D_{\text{eff}} = D_l + D_t$. The eddy components are given by

$$\mu_t = \frac{C_\mu \rho K^2}{\epsilon} \ , \ \lambda_t = \frac{\mu c_p}{\mathrm{Pr}_t} \ , \ D_t = \frac{\mu_t}{\rho\, \mathrm{Sc}_t} \ ,$$

where K is the turbulence kinetic energy, ϵ the dissipation rate of the turbulence kinetic energy, Pr$= c_p\mu_t/\lambda_t$ the turbulent Prandtl number and Sc$= \mu_t/(\rho D_l)$ the turbulent Schmidt number. To find K and ϵ, two further differential equations have to be solved

$$\rho \frac{D}{Dt} K = G - \rho\epsilon + \vec{\nabla} \cdot \left[\left(\mu_l + \frac{\mu_t}{s_K} \right) \vec{\nabla}\, K \right]$$

and

$$\rho \frac{D}{Dt} \epsilon = C_1 G \frac{\epsilon}{K} - C_2 \rho \frac{\epsilon^2}{K} + \vec{\nabla} \cdot \left[\left(\mu_l + \frac{\mu_t}{s_\epsilon} \right) \vec{\nabla}\, \epsilon \right]$$

where

$$G = 2\mu_t \left[\left(\frac{\partial v_r}{\partial r} \right)^2 + \frac{v_r^2}{r} + \left(\frac{\partial v_z}{\partial z} \right)^2 \right] + \mu_t \left\{ \left(\frac{\partial v_z}{\partial r} + \frac{\partial v_r}{\partial z} \right)^2 + \left[r \frac{\partial}{\partial r} \left(\frac{v_\theta}{r} \right) \right]^2 \right\} .$$

C_1	C_2	s_K	s_ϵ	C_μ	Pr_t	Sc_t
1.44	1.92	1.0	1.3	0.09	0.9	0.9

Table 1: $K-\epsilon$ turbulence parameters for pipe flows [LS72].

For the flow inside the plasma torch, model paramters are given in table 1. However, due to the large variations of molecular viscosity in the plasma, both laminar and turbulent regimes may be present in the same flow. To account for that, it was proposed to expand the form of the K-ϵ-model by making the empirical constants functions of the Reynolds number of turbulence [LS74a]. In [MK93], the constants C_μ and C_2 in the arc plume are modified due to Rodi [Rod72]:

$$C_\mu = 0.09 - 0.04f \ , \ C_2 = 1.92 - 0.0667f \ ,$$

where

$$f = \left| \frac{\delta}{2\Delta u} \left(\frac{\partial v_{z,0}}{\partial z} - \left| \frac{\partial v_{z,0}}{\partial z} \right| \right) \right|^{0.2} .$$

δ is the plume diameter, Δu is the difference between center line and free stream velocity, and $v_{z,0}$ is the center line velocity.
Formulating boundary conditions for the K-ϵ turbulence parameters is rather complex. Murphy sets K=ϵ=0 at the outflow boundary and $\partial K/\partial z$=$\partial \epsilon/\partial z$ = 0 at the anode surface. At the inlet of the nozzle, where the flow is treated laminar, they use $K_{in} = i_t \left(v_r^2 + v_\theta^2 + v_z^2\right)$ and $\epsilon_{in} = 3K_{in}^{3/2}/R$ where i_t is the turbulence intensity, taken to be 0.003, and R is the radius of the inlet to the nozzle. Additionally the wall function approach is used [MK93].

2.4 Solution methods

The system of nonlinear partial differential equations decribing the arc column has to be solved by numerical methods. Attempts to find analytical solutions by drastic simplification have been made (see e.g. [Den62]), but are of limited practical importance to welding arc situtations. Current numerical methods solve the column equations in two dimensions assuming radial symmetry of the arc. The medium sized (5000-50000 lines of code) computer programs to perform the calculations are mainly based on the SIMPLE algorithm of Patankar [PS72], i.e. the solution is obtained from a control-volume formulation based finite difference method (FDM). Finite element method (FEM) based calculations are actually not known and available codes can unlikely deal with such complicated equations. Recently, a commericial FDM code was used, but most groups use proprietrary developments. Code development times between 2 and 20 man years are usual.
Details on the method can be found in Patankars famous book [Pat80]. After writing the system of non-linear partial differential equations in the generalized form

$$\frac{\partial}{\partial t}(\rho\Phi) + \vec{\nabla}\cdot(\rho\vec{\mathbf{v}}\Phi) = \vec{\nabla}\cdot\Gamma_\Phi\vec{\nabla}\,\Phi + S_\Phi \tag{19}$$

where

physical quantity	Φ	Diffusity Γ_Φ	Source S_Φ
mass	1	0	0
momentum	v_i	μ	...
enthalpy	h	λ	...
...	...	...	...

,

the implementation is straightforward, but very work intensive and requiring excellent numerical abilities, especially for proprietary numerical grid generators.
On current engineering workstations (50 MFLOPS[4], accurate column calculations can be performed with less than 1 hour CPU-time and about 2 MB RAM, using a 100x100 non-equidistant numerical grid. The codes acually known all use the single grid approach and (in most cases) a line-by-line solver for the discretisation matrix. Several hundred iterations are required to reach the steady state. Three dimensional modelling will require much more memory (above 64 MB) and a change in the algorithms, because the single-grid approach means the CPU-time scales with $O(n^2)$, where n is the number of unknowns (grid points). Such quadratic scaling can make 3D-calculations impossible, while modern multigrid methods may show linear scaling [Bra84, Hac85].
Including electrode sheath models and high pressure or turbulence effects, arc modelling is often limited by convergence problems.

3 Theory of the electrode regions

Understanding and predicition of arc electrode processes is a matter enormous research efforts since several decades (see e.g. [Eck61], 630 ref's and [Gui71], 238 ref's and [Gui84], 616 ref's). For this review, we concentrate on the presentation of a mathematical model, which may be used for accurate handling of these thin nonequilibrium layers within future welding arc simulations. The cathode phenomena are presented in more detail, because the anode is mainly described by a similar model.

3.1 Cathode phenomena

3.1.1 Introduction

The description of the non-equilibrium plasma in front of an electron emitting metal surface is of high importance for theoretical investigations of thermal plasma arcs in many applications, because suitable boundary conditions at the electrodes are of crucial importance for modelling the overall discharge [Gui84, JSCQ94]. This section is aimed to develop a model which yields cathode boundary conditions for arc column modelling. Based on the well accepted division of the high intensity arc discharge into cathode region (figure 9), flow affected arc column and anode boundary layer (see figure 3), this section deals with the detailed description of the so called cathode fall. The work of Hsu and Pfender [HP83a] is extended to allow self-consistent linking of ionization- and space-charge-zone and computation of the overall voltage drop [Ret94, RKT$^+$95, RWKS96]. The transition between space-charge- (sheath) and ionization-zone (presheath) is approximated by a sharp boundary, called sheathedge [Rie91]. While the sheath is assumed

[4] Million floating point operations per second.

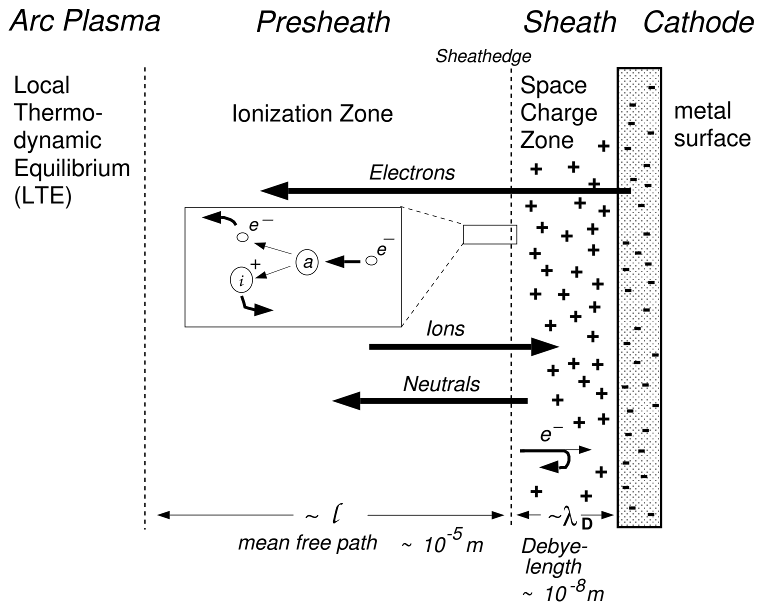

Figure 9: Conditions in an arc plasma near an electron emitting metal surface.

to be collision free, the presheath is governed by a number of collision processes and quasineutrality:

Ionization zone (Presheath)	Space-Charge Zone (Sheath)	Cathode surface
collision dominated, 3 particle species, 2 temperature treatment, constant total pressure, quasineutral	collision free, monoenergetic treatment, space charges	solid body, thermionic emitter

The electrons emitted by the cathode surface are accelerated by the sheath potential drop. Within the presheath, energy transfer between this beam of emitted electrons and the heavy particles takes place. Ionization and electron-ion collisions determine the typical scale of the presheath extension. At the plasma side of the presheath, the arc plasma is in local thermodynamic equilibrium (LTE).
Recently, Morrow developed a model of the presheath [LMZ+93], which Zhu included into the calculation of the arc column [ZLM92]. Together with [DS90], this work is the first attempt towards a self-consistent computation of cathode boundary conditions for arc column modelling, rather than making assumptions on the cathode current-density and plasma temperature [JSCQ94]. In [LMZ+93, ZLM92, DS90], the approximation of equal electron- and heavy-particles-temperature was used. Because their presheath treatment was of the so-called Schottky type [Sch24], the effects of space-charge formation were neglected. As the potential drop within this sheath may be about two thirds of the overal cathode potential drop, the present work is aimed to a more accurate description of this region.

The first integrated analysis of the ionization-zone by Hsu and Pfender [HP83a] formed the starting point of this work. After summarizing their presheath model, we compute the sheath potential drop. The Bohm criterion is applied to link sheath and presheath to an unique model.

3.1.2 The presheath

The ionization-zone is assumed to be quasineutral and consisting of three compounds: electrons (index e), single positive charged ions (index i) and neutrals (index a). The latter are described by a single fluid of heavy particles (index h). The behaviour of these separate species is illustrated in figure 9. After the fundamental work of Hoffert and Lien [HL67], Hsu and Pfender [HP83a, Hsu82] developed a model of the presheath, which is applied in this work. The role of the individual terms was already discussed [HP83a], therefore only a brief summary of the model is given below.

In the two-fluid description, the continuity equations for the electrons and ions read

$$\vec{\nabla}\cdot\vec{\Gamma}_e = \vec{\nabla}\cdot(n_e\vec{u}_e) = \dot{n}_e \quad \text{and} \tag{20}$$
$$\vec{\nabla}\cdot\vec{\Gamma}_i = \vec{\nabla}\cdot(n_e\vec{u}_i) = \dot{n}_e \ , \tag{21}$$

where equal electron and ion number density (quasineutrality: $n_e = n_i$) is applied. $\vec{\Gamma}_{e,i}$ denotes the fluxes and $\vec{u}_{e,i}$ the drift velocities of the electrons and ions. The net ionization rate

$$\dot{n}_e = \alpha_{\rm rec}\, n_e^3 \cdot \left(\frac{n_a}{n_{a,\rm LTE}} - 1\right) \tag{22}$$

is determined from the three body recombination coefficient $\alpha_{\rm rec}$ [HL67] and a *near equilibrium* ionization rate. The equilibrium density of neutrals $n_{a,\rm LTE}$ is given by the generalized Saha equation (14). In the one-dimensional treatment, equations (20) and (21) include the condition of constant electric current density. The electron and ion fluxes are obtained by a modified Chapman Enskog approach [HCB64, Dev67a] to

$$\vec{\Gamma}_e = n_e\vec{u}_e = -\left(\frac{D_e^T}{m_e T_e} + \frac{m_e n\, n_e D_{ee}}{\rho\, T_e}\right)\vec{\nabla}\, T_e - \frac{m_e n}{\rho} D_{ee}\vec{\nabla}\, n_e + \frac{m_e n\, n_e}{\rho\, k_{\rm b} T_e} D_{ee}\, e\vec{\nabla}\, V \tag{23}$$

and

$$\vec{\Gamma}_i = n_e\vec{u}_i = -\frac{n_a\, m_a\, D_{ia}}{\rho}\vec{\nabla}\, n_e + \frac{n_e\, m_i\, D_{ia}}{\rho}\vec{\nabla}\, n_a - \frac{n^2 n_e\, m_i\, D_{ia}}{p\,\rho}\, e\,\vec{\nabla}\, V \ . \tag{24}$$

V is the electric potential, $T_{e,i,h}$ the temperature, $m_{e,i,h}$ the mass of the individual species, $\rho = \sum_{\xi=e,i,a} n_\xi m_\xi$ the overall mass density, $n = \sum_{\xi=e,i,a} n_\xi$ the total density and $p = \sum_{\xi=e,i,a} n_\xi k T_\xi$ denotes pressure. Within the presheath, the individual contributions to total pressure (e, i, a) are changing significantly. At the plasma side, p is given by p_e and p_i, while at the sheath edge, mainly p_e and p_a contribute to the total pressure.

In the absence of net mass flow, the ion and neutral diffusion fluxes are linked by $\vec{\Gamma}_i = -\vec{\Gamma}_a$. In eqn. (23) and (24), D_e^T denotes the thermal diffusion coefficient of the electrons and D_{ia} the ordinary diffusion coefficient between ions and neutral atoms, both taken from the work of Ahtye [Aht65]. The electron self diffusion coefficient D_{ee} is linked to the two-temperature electrical conductivity σ by

$$D_{ee} = \frac{\rho\, k_{\rm b}\, T_e}{m_e\, n\, n_e\, e^2}\,\sigma \ . \tag{25}$$

σ was taken from Kannapan's work [KB77]. Because of the small thermal diffusion coefficient of the ions D_i^T [Aht65], the corresponding term can be neglected.
Decoupling of electron and heavy particles temperature is one of the most important effects in the ionization-zone, i.e. their energy conservation equations must be given separately. The energy balance of the electrons becomes

$$e\vec{\Gamma}_e \cdot \vec{\nabla} V = -\vec{\nabla} \cdot (\lambda_e \vec{\nabla} T_e) + {}^5\!/_2\ k_\mathrm{b}\, \alpha\, \vec{\Gamma}_e \cdot \vec{\nabla} T_e + \left({}^5\!/_2\ k_\mathrm{b} T_e\, \alpha + E_\mathrm{ion}\right) \dot{n}_e + W_{eh} \tag{26}$$

with

$$\alpha = 1 + 2\rho\, D_e^T / (5\, n_e\, n\, m_e m_a D_{ee}) \ .$$

The last term denotes the energy loss due to elastic collisions with the heavy particles, given by

$$W_{eh} = n_e\, {}^3\!/_2\ k_\mathrm{b} \frac{2m_e}{m_a} \cdot (T_e - T_h) \cdot (n_a Q_{ea} + n_e Q_{ei}) \cdot v_e^\mathrm{th} \ . \tag{27}$$

v_ξ^th denotes the mean thermal velocity of the fluid species. The electron-atom cross section Q_{ea} was taken from [Dev67b] and the electron-ion cross section Q_{ei} from [Bal88]. Radiation losses can be neglected as they give only a very small contribution [HP83a]. The thermal conductivity of the electrons is calculated with the Chapman Enskog approach [Dev67a], yielding [Ret94]

$$\lambda_e \simeq 6.32 \cdot 10^{-19}\, n_e \sqrt{T_e}\, \frac{1}{n_e\, \tilde{Q}_\mathrm{Coul} + n_a\, \tilde{Q}_{ea}} \quad \frac{\mathrm{m}^2}{\sqrt{\mathrm{K}}} \quad \frac{\mathrm{W}}{\mathrm{m\,K}} \ ,$$

where $\tilde{Q}_\mathrm{Coul}$ and $\tilde{Q}_{ea}$ denote the linear combination of the considered collision integrals (second order approximation) for coulomb- and for electron-neutrals collisions, respectively. For the cross sections, we found the fit formula

$$\tilde{Q}_{ea} \simeq \left\{51.6 - 1.23 \cdot 10^{-3}\, \frac{T_e}{\mathrm{K}} + 0.25 \exp\left(\frac{T_e}{10^4\mathrm{K}}\right) - 55.3 \exp\left(-\frac{T_e}{10^4\,\mathrm{K}}\right) \mathrm{K}\right\} \cdot 10^{-20}\,\mathrm{m}^2 \ , \tag{28}$$

and

$$\tilde{Q}_\mathrm{Coul} \simeq 1.46 \cdot 10^{-9}\, \ln\left(T_e/891\,\mathrm{K}\right)\, T_e^{-2} \quad \mathrm{K}^2\,\mathrm{m}^2. \tag{29}$$

The energy balance of the heavy particles becomes

$$-\, e\vec{\Gamma}_i \cdot \vec{\nabla} V + W_{eh} = -\vec{\nabla} \cdot (\lambda_h \vec{\nabla} T_h) \ . \tag{30}$$

The heavy particles thermal conductivity $\lambda_h = \lambda_i + \lambda_a$ was obtained by the relaxation time approach as

$$\begin{aligned} \lambda_i &= {}^5\!/_2\ k_\mathrm{b}\, n_i\, v_i^\mathrm{th}\, (n_i\, Q_{ii} + n_a\, Q_{ia})^{-1} \\ \lambda_a &= {}^5\!/_2\ k_\mathrm{b}\, n_a\, v_a^\mathrm{th}\, (n_a\, Q_{aa} + n_i\, Q_{ia})^{-1} \end{aligned}$$

where the ion-ion cross section Q_{ii} was taken from [Bal88], Q_{ia} for ion-atom charge exchange collisions from [And90] and $Q_{aa} \simeq 0.973 \cdot 10^{-19}\mathrm{m}^2$.
The presheath equations (20), (21), (23), (24), (26) and (30) are closed by the assumption of constant thermal pressure. For an one-dimensional treatment of the cathode zones, they are solved numerically using Bulirsch-Stoer method [PTV+92]. As a result, we obtain the quantities n_e, n_a, T_e, T_h, u_e and u_i.

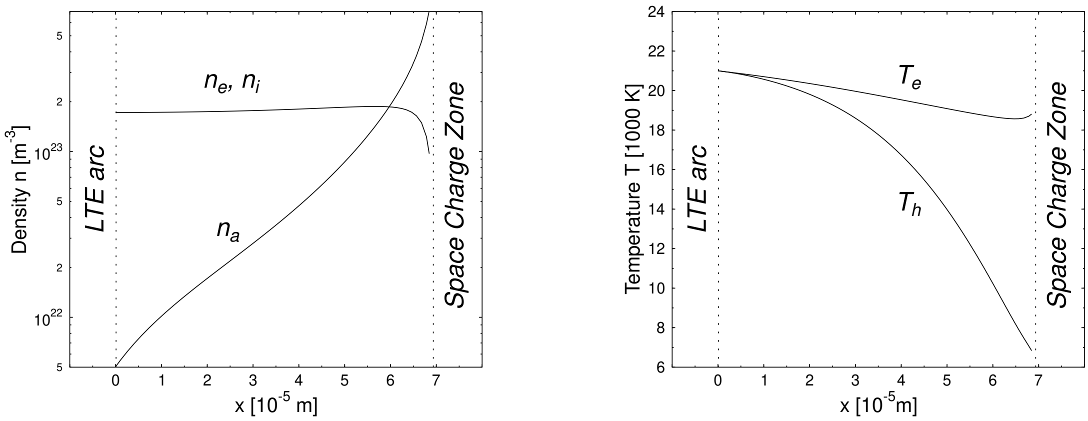

Figure 10: Spatial dependence of particle densities $n_e = n_i$ and n_a (left), and electron temperature T_e and heavy particles temperature T_h in the presheath (right) [RWKS96].

The presheath-only computation were carried out for Hsu's boundary conditions [HP83a] at the plasma side:

$$\begin{aligned} T_e &= T_h = 21000 \text{ K} \\ V &= 8.5 \text{ V} \\ \frac{d}{dx} n_e &= 1.692 \cdot 10^{24} \text{ m}^{-4} \\ \frac{d}{dx} V &= -1.45 \cdot 10^4 \text{ V/m} \ . \end{aligned}$$

Furthermore, the value for the constant electrical current density is chosen as $j_{\text{tot}} = 1.2 \cdot 10^8$ A/m^2 and the constant thermal pressure is assumed to be atmospheric.
On the cathode side of the presheath, a new boundary condition was introduced, the so-called Bohm criterion [Boh49]:

$$u_i = u_{\text{Bohm}} := \sqrt{\frac{k_{\text{b}} T_e}{m_i}} \ . \tag{31}$$

As discussed in detail by Riemann [Rie91], this criterion is sufficient for space charge sheath formation and physically justified, whereas Hsu's criterion was of more qualitative nature.
The spatial dependence of the particle densities and temperatures are shown in figure 10. The results can be explained considering the electrons emitted from the cathode surface entering the presheath from the right side of the figures. These electrons have a high velocity as they have been accelerated in the sheath potential. Ionization occurs in collisions with neutrals. Therefore, the electron and ion densities increase, while the neutral atom density decreases. Because the electrons equilibrate on a much shorter scale, thermal equilibrium of the electron gas at the sheathedge can be assumed. The scale for thermal relaxation of electrons and heavy particles should be a few mean free paths for electron-heavy particle collisions. As we found the mean free path for electron-ion collisions to be about $\ell_{ei} \approx 10^{-5}$ m the extension of the presheath of $d_{PS} \approx 7 \cdot 10^{-5}$ m is in good agreement.

3.1.3 The sheath

The main idea of our space-charge-zone (sheath) calculation is to determine the sheath potential drop from the boundary conditions at the cathode surface and at the sheath-edge, rather than making an assumption on this value. The densities within the sheath and its extension may be computed by the simplified model of monoenergetic ions [PA76], or direct solution of Vlasov's and Poisson's equation. However, these information are not of primary importance for the overall calculation of the cathode fall.

The total electric current density j_{tot} in the sheath consists of three terms: The current density of the electrons emitted from the cathode surface j_c and accelerated within the sheath, the current density of the ions accelerated towards the cathode j_i and the current density of the plasma electrons j_p repelled by the sheath potential, but having enough energy to reach the cathode surface. With the x-axis towards the cathode surface, the partial electric current densities j_c and j_i are positive, j_p is negative. Since the sheath is collision free, each of the current densities is constant.

Field emission is assumed to be negligible, j_c is therefore given by Richardson's formula

$$j_c = j_{\mathrm{Rich}}(T_C, \Phi_C) = A_{\mathrm{Rich}}\, T_C^2 \, \exp\left(-\frac{\Phi_C}{k_{\mathrm{b}}\, T_C}\right) \quad , \tag{32}$$

where A_{Rich} is Richardson's constant, T_C the cathode surface temperature and Φ_C the effective work function of the cathode material. Thus, the density of emission electrons at the sheathedge becomes

$$n_{c,SE} = \frac{j_c}{e}\sqrt{\frac{m_e}{2}}\,\left(2k_{\mathrm{b}}T_C + eV_{SE}\right)^{-1/2} \quad , \tag{33}$$

where $2k_{\mathrm{b}}T_C$ denotes the mean energy of the emitted electrons and eV_{SE} the additional energy after acceleration in the sheath potential.

To calculate the current density of the ions, two assumptions can be made. First, the ions are treated as monoenergetic particles, entering the sheathedge with Bohm's velocity (31). Additionally it is assumed that all ions recombine at the cathode surface. Then j_i becomes

$$j_i = e\, n_{e,SE}\, u_{\mathrm{Bohm}} = e\, n_{e,SE}\sqrt{\frac{k\, T_{e,SE}}{m_i}}. \tag{34}$$

$T_{e,SE}$ denotes the electron temperature and $n_{e,SE}$ the ion density at the sheathedge.

Only the plasma electrons with an individual velocity above $v_{\min} = +\sqrt{2eV_{SE}/m_e}$ contribute to j_p. The velocity distribution of the plasma electrons at the sheathedge is assumed to be maxwellian, therefore j_p becomes

$$j_p = -e\, n_{p,SE}\sqrt{\frac{k_{\mathrm{b}}T_{e,SE}}{2\pi m_e}}\, \exp\left(-\frac{eV_{SE}}{k_{\mathrm{b}}T_{e,SE}}\right) \tag{35}$$

where $n_{p,SE} = n_{e,SE} - n_{c,SE}$ is the density of plasma electrons at the sheathedge. Finally, the total electric current density

$$j_{\mathrm{tot}} = j_c + j_i + j_p \tag{36}$$

provides an implicit equation for the sheath potential drop V_{SE}, depending on cathode temperature T_C, work function Φ_C, total current density j_{tot}, electron density $n_{e,SE}$ and electron temperature $T_{e,SE}$ at the sheathedge.

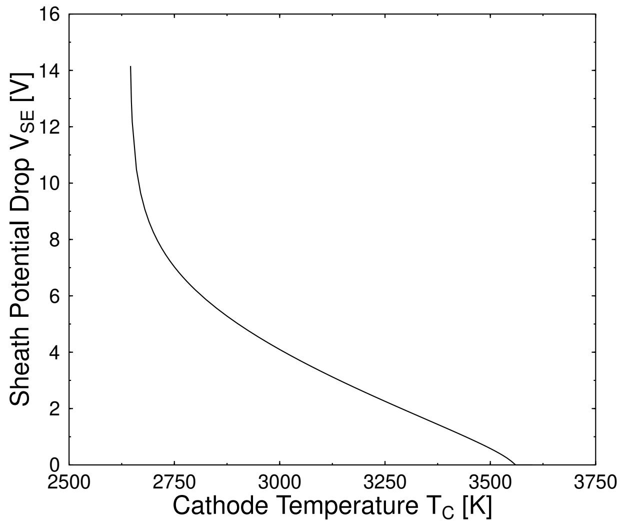

Figure 11: Sheathpotential in dependence on the cathode temperature [RWKS96].

As an example, figure 11 shows the variation of V_{SE} with cathode temperature T_C for a typical argon arc situation ($n_{e,SE} = 1.2 \cdot 10^{23}$ m^{-3}, $T_{e,SE} = 19000$ K, $j_{\text{tot}} = 1.2 \cdot 10^8$ A/m^2 and $\Phi_C = 2.63$ eV). When the cathode temperature T_C is too low, the current density of the emission electrons is very small. Even for a vanishing current density of the plasma electrons $j_p = 0$, the given total current density j_{tot} cannot be reached. A vanishing j_p is equivalent to an infinite sheathpotential $V_{SE} = \infty$. In the opposite case, when the cathode temperature T_C exceeds a certain value, the current density of the emission electrons is very high. The maximum possible j_p is not sufficient to compensate the high sum $j_c + j_i$, to achieve the given total current density $j_{\text{tot}} = j_c + j_i + j_p$. In most cases (when $n_{c,SE} \ll n_{p,SE}$) the maximum j_p is reached for a zero sheath potential drop. These existence areas provide a physical mechanism for current limitation by space charge sheath formation.

3.1.4 Overall solution method

For the present model, the temperature of the cathode surface T_C, the effective work function of the cathode material Φ_C, the constant electric current density j_{tot} and the constant thermal pressure p in the calculation region are prescribed. In a certain distance d_{tot} from the cathode surface, the plasma temperature T_P and its gradient ∇T_P are boundary conditions as well. This situtation is illustrated in figure 12.
The iterative calculation starts with the computation of the presheath properties, assuming the arc boundary of the presheath at position P in figure 12. For the presheath calculation as described in section 3.1.2, additional boundary conditions at the plasma side are needed. The gradient of the electron density can be calculated in one-dimensional local thermodynamic equilibrium with help of the Saha equation (14). The electric field

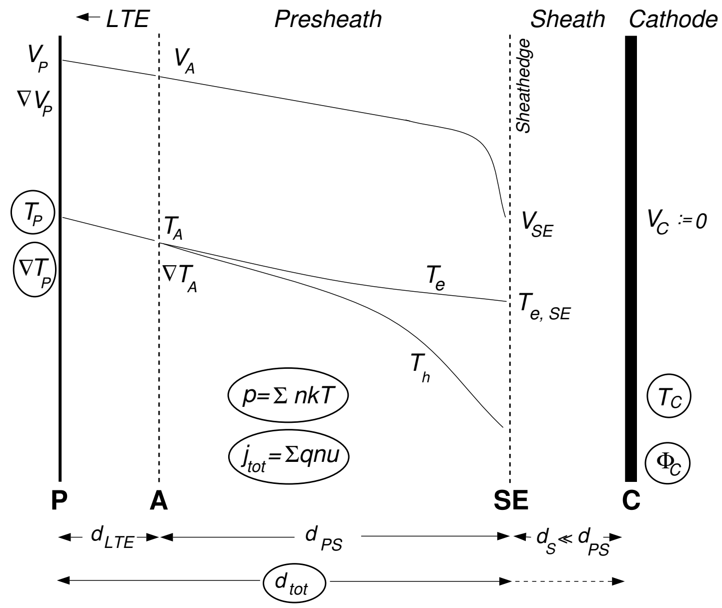

Figure 12: Geometry of the computation region. The boundary conditions for the final entire calculation of the transition cathode–equilibrium plasma are encircled. Additionally, the distribution of the potential and the temperatures in the presheath are shown.

in the plasma ∇V_P results self-consistently. With an arbitrary chosen potential drop $\tilde{V}_P$ all necessary boundary conditions for the presheath calculation are given. The resulting presheath extension d_{PS} is assumed to be smaller than the given overall distance d_{tot}. Since the sheaths extension d_S is negligible on this scale, the difference is assumed to be a LTE region. Now the presheath calculation has to start at position A in figure 12, therefore its boundary conditions (T_A and ∇T_A) must be calculated anew. This can be done with the assumption of constant the electric field within the LTE region. With iterative calculations we achieve that the sum of d_{LTE} and the resulting d_{PS} does not differ from the given d_{tot} more than 10^{-8} m. This is a suitable condition as it is the order of magnitude of the sheath's extension.
For the calculation of the potential drop in the sheath V_{SE} we use the electron density $n_{e,SE}$ and electron temperature $T_{e,SE}$ obtained by the presheath calculation. With the knowledge of the sheath potential V_{SE} and the potential drop in the presheath the randomly chosen overall potential drop $\tilde{V}_P$ can be adjusted to the real value V_P. Also the potential drop over the nonequilibrium region V_A is obtained. Additional results are the electric field on the plasma side of the nonequilibrium region, the real extension of the nonequilibrium region and the net energy flux density towards the cathode surface q_C. Neglecting cathode evaporation and radiation, q_C results from ion and electron heating and electron emission cooling

$$q_C = j_i \cdot \left(V_{SE} + \frac{E_{ion} - \Phi_C}{e} \right) - (j_P + j_{\mathrm{Rich}}) \cdot \frac{\Phi_C}{e} \tag{37}$$

This net energy flux density towards the cathode surface is balanced by heat conduction into the solid. Moreover, there exists an important ohmic contribution to the overall heating of the cathode body.

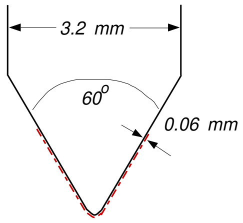

Figure 13: A typical cathode tip of a TIG welding arc, with the nonequilibrium region in its true scale.

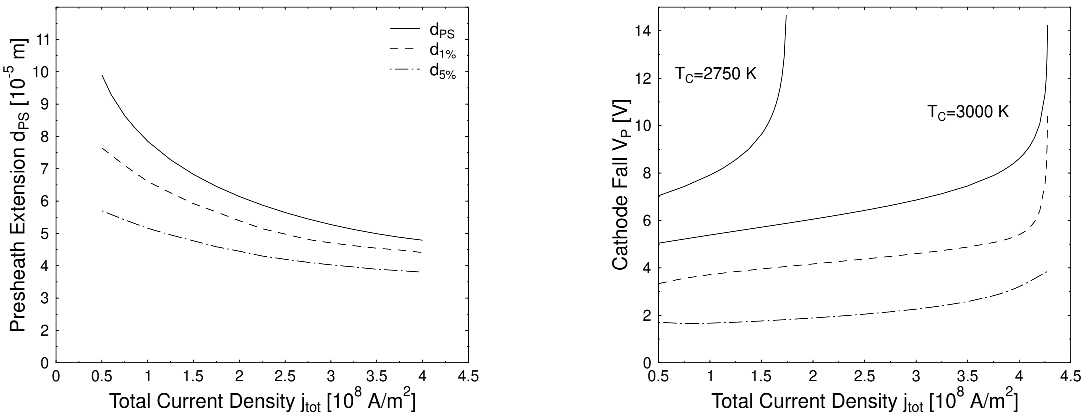

Figure 14: Extension of the nonequilibrium region (left: —— $T_e = T_h$, - - - $T_e \simeq_{1\%} T_h$ and –·–·–· $T_e \simeq_{5\%} T_h$) and potential drop over the non-equilibrium region plotted against total electric current density (right, —— for two different cathode temperatures; for $T_C = 3000$ K the sheath (- - -) and presheath (–·–·–·) potential drop are shown separately) [RWKS96].

3.1.5 Results and discussion

The results are shown for the following typical boundary conditions, the notation can be seen in figure 12:

$$\begin{aligned} T_P &= 21000 \text{ K}, \\ \frac{d}{dx} T_P &= -2.7 \cdot 10^7 \text{ K/m}, \\ p &= 1.013 \cdot 10^5 \text{ Pa}, \\ d_{\text{tot}} &= 1 \cdot 10^{-4} \text{ m} \\ \text{and} \quad \Phi_C &= 2.63 \text{ eV (thoriated tungsten).} \\ \text{Additionally} \quad T_C &= 3000 \text{ K} \\ \text{or} \quad j_{\text{tot}} &= 1.2 \cdot 10^8 \text{ A/m}^2 \;, \quad \text{respectively.} \end{aligned}$$

From this boundary conditions, we obtain an extension of the nonequilibrium region of $d_{PS} \approx 6 \cdot 10^{-5}$ m. For the case of a TIG welding arc, the one-dimensional treatment is justified (figure 13). For the integration of this locally one dimensional model into the overall two dimensional arc calculation, Zhu's iteration procedure may be used [ZLM92]. The extension of the nonequilibrium region d_{PS} in dependence of the total electric current

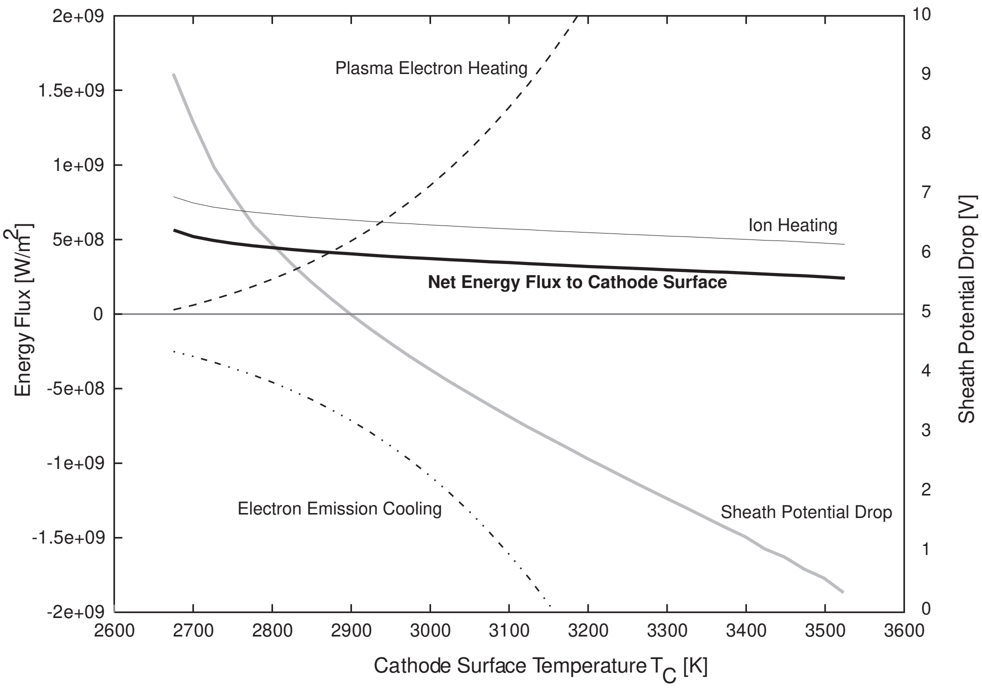

Figure 15: Net energy flux density towards the cathode surface after equation 37 for a constant current density of $1.2{\cdot}10^8\,\mathrm{A/m^2}$ plotted against cathode surface temperature. The individual contributions and the corresponding sheath potential drop are also shown.

density j_{tot} is shown in figure 14 for various definitions of temperature equilibrium. The figure shows a larger extension of the nonequilibrium region for lower electric current densities j_{tot}. This can be explained with the lower electron number density n_e resulting from the presheath calculation for lower j_{tot}. Decreasing electron density means less energy supplied to the heavy particles, thus covering a longer distance before temperature equilibrium is reached.

Calculated from equation (37), the net energy flux density towards the cathode surface is shown in figure 15. In order to sustain the prescribed current density of $1.2{\cdot}10^8\,\mathrm{A/m^2}$, the sheath potential drop decreases with temperature and thus the cooling due to electron emission is mainly balanced by the heating of the reverse electron current.

One of the main results is the overall cathode potential drop (cathode fall), which is obtained self-consistently with the integrated sheath- and presheath-model described above. As a function of the net current density, its value is shown in figure 14. Fixing the other boundary conditions, the cathode potential drop increases with total electric current density j_{tot}. Above a specific current density threshold, no solution exists for a given cathode temperature. For a cathode temperature of $T_C = 3000$ K the individual sheath and presheath contributions are also plotted. As mentioned in section 3, the space-charge-zone is responsible for the current limitation.

3.1.6 Summary

A one-dimensional model for the calculation of the transition from an electron emitting cathode surface to the local thermodynamic equilibrium (LTE) arc plasma was presented [Ret94, RKT+95, RWKS96]. We described the presheath by a hydrodynamic model, considering ionization and transport processes. Compared to models treating the ionization zone as a black box described by averaged quantities [ZHP94, UFT94], spatial variation of the physical quantities and decoupling of electron- and heavy particle-temperatures were taken into account. The calculation of the space-charge-zone yields the sheath potential drop, by considering electron emission at the cathode surface and the physical properties of the collision free sheath. This also leads to existence areas for the overall non equilibrium region. The link of sheath and presheath was done by introducing Bohm's criterion. In contrast to [HP83a], the space-charge- and ionization-zone were connected, using boundary conditions from the LTE-side as well as from the cathode, but without requiring the potential drop as a prescribed quantity.

3.2 Anode phenomena

Anode phenomena at atmospheric arcs were studied since several decades [BPF54, BH54, BH55, BH56b, BPF55, HB55, Sch63, BH56a]. In general, one has to distinguish between modelling of the near anode arc colum, often also stated as anode modelling [CP80, CP81, SEHP82], and modelling of the thin non-equilibrium layer in front of the active anode area, as defined by Pfender [Pfe80]:
The *anode diffusion layer* is defined as the zone in front of the anode which is affected by the presence of the low temperature anode. For welding arc situations, this layer has a thickness in the order of 0.1mm which is substantially larger than the mean free path length of the electrons. Therefore, this layer may be treated as a continuum.
The steep gradients of temperature and particle densities in this zone give rise to diffusional fluxes which must be considered in the governing equations. The heavy particle temperature, for example, drops in this zone from the plasma temperature to anode surface temperature. If LTE would prevail throughout this zone, the electrical conductivity would be almost zero in front of the anode, violating the requirement of current continuity. This implies that the electron temperature must be substantially higher than the heavy particle temperature, i.e. there will be appreciable deviations from LTE within the anode boundary layer.
As previously mentioned, there is another layer located at the bottom of the anode boundary layer overlying the anode surface, known as the sheath. The thickness of this sheath is several orders of magnitude less than the thickness of the anode boundary layer. In general, the anode fall is identified with the potential drop across the sheath because within the sheath there are strong electric fields due to deviations from quasi-neutrality. In general, modelling of the anode layer is similar to the cathode modelling described in section 3.1. Anode layer models actually included into overall arc modelling codes are in fact indentical to the corresponding cathode layer models [ZLMH95].

3.2.1 Modelling anode layer effects

A number of one dimensional treatments of the anode fall can be found in literature, e.g. [NP77] computes a current density dependence of the anode fall voltage V_a. Nazarenko's model predicts a potential hump [NP89], and Nemchinskij describes the MIG-welding electrode [Nem94].
For welding application, the arc excess pressure will remain constant within the small anode boundary layer, and can thus be deducted from the column modelling result. The

energy flow is in fact influenced by the anode fall. Without taking the details of the anode fall into account, most authors assume an anode fall voltage and deduce the energy flow from Dinulescu's formula [DP80]:

$$q_a = q_{a,elec} + q_{a,conv} + q_{a,rad}$$

where the (dominating) electronic contribution is given by

$$q_{a,elec} = j_a \left(\frac{5}{2} + \frac{eD_e^T}{k_\mathrm{b}\sigma_e} \right) \frac{k_\mathrm{b} T_{a,elec}}{e} + j_a \Phi_{\mathrm{eff},a} + j_a V_a$$

for $V_a > 0$. The term in parentheses was found to be approximately 3.203, thus assuming an electron temperature of 10^4K at the anode, one can simply use

$$q_{a,elec} = j_a (2.76 + \Phi_{\mathrm{eff},a})$$

where $\Phi_{\mathrm{eff},a}$ is the effective work function of the anode material (4.3(Cu)...4.5(steel)). The radiative contribution has to be computed, by integrating over the arc column:

$$q_{a,rad} = q_{rad,i,j} = \int_{V_j} \frac{S_{R,i,j}}{4\pi r_{i,j}^2} \cos\psi dV_j,$$

and the convective term is given by [MS86]:

$$q_{a,conv} = \frac{0.515}{\mathrm{Pr}_w} \left(\frac{\mu_e \rho_e}{\mu_w \rho_w} \right)^{0.11} \left(\mu_w \rho_w \frac{du_e}{dr} \right)^{0.5} (h_e - h_w)$$

where subsript e denotes the value at the anode end of the arc column (anode layer edge) and w the values at the wall.
From these heat flow distributions, one can determine the arc efficiency

$$\eta = \frac{2\pi \int_0^{L_r} q_a r dr}{I(V_c + V_{col} + V_a)},$$

a formula normally applied without taking the unknown anode fall voltage V_a into account. Actually, the modelling results do not provide an arc efficiency formula suitable for pratical purposes, thus Ghents formula estimated from experiments may be used [GRH+79]:

$$\eta = 0.96 - 0.12 \cdot P_{tot}[kW] \ , \ P_{tot} = V_{tot} \cdot I.$$

3.2.2 Experimental data

The fact, arc voltage changes with anode composition is even known from earlier experimental work [CS71]. Electric probe measurements have been performed at and close to a plane, water-cooled anode surface in atmospheric pressure, high intensity argon arcs [SP84] for different arc configurations which in turn, result in two distinctly different anode arc roots (diffuse and constricted). An adjustable fine wire probe penetrating through a small hole in the center of a flat anode allows for potential and electron temperature measurements in the anode boundary layer. For the parameter range covered by this investigation (100A $< I <$ 250 A) the results reveal negative anode falls ranging

from approximately -2.1 to -1.4 V. Electron temperatures at the anode surface range from 8800 to 9800K. Calorimetric energy balances from which the contributions of the various modes of heat transfer to the anode may be derived, indicate the importance of convective heat transfer to the anode. The results of the calorimetric studies as well as of the anode fall measurements are consistent with an anode heat transfer model which takes negative anode falls into account.
Recent Langmuir probe experiments found anode drops between +3V for pure argon arcs and +5V for pure helium arcs [ZH94]. These measurements are also in good agreement with other authors, as summarized in [HM94].

3.2.3 Anode modes

For pratical welding applications it is of major importance to get high energy densities at high welding speeds. As investigated by Kimblin on copper anodes and arcs in air, there may occur stable continous anode attachment or a jumping anode spot [RS71], depending on arc parameters like current and arc length. Similar observations where reported by Guile for argon arcs on stainless steel anodes [CG77], and recently for Ar-He arcs [IIOY94].
For high speed welding application, such phenomena will need time dependent and three dimensional arc models, currently not available. Thus application of current modelling is restricted to smaller welding speeds, i.e. below 0.5m/min and perpendicular incidence of the cathode.

3.3 Summary of electrode modelling

Currently, determination of the anode fall voltage and the exact properties of the anode diffusion layer and space charge sheath (which in fact is responsible for the potential drop), is not available. Additionally, one has to include metal evaporation from the weld pool surface into account, e.g. by a Langmuir-type evaporation model [CS92].
Remarkably, neglecting space charge sheath effects [ZLMH95] may also lead to total arc voltages similar to the measured ones: The positive cathode space charge sheath potential drop may be comparative to the negative anode voltage drop, thus producing only a small error in overall arc voltage, when neglecting both. Morrow's presheath model [LMZ+93], which does not include the important temperature split effect or space charge sheath formation, is in fact the first one really applied to the computation of the arc itself. The situation may become more clear, when including a sheath and presheath type model based on the equations given in section 3.1 into the overall arc calculation.
Heat conduction within the electrodes is straightforward, and was not reviewed here.

4 TIG arc modelling results

Two dimensional numerical modelling of free burning argon arcs has made significant progress since introduced by Pfender's group (see table 2). While modelling of the *real* TIG arcing during welding operation is still not possible, usually argon arcs burning stationary on a cooled copper anode are modelled.
Such modelling can be compared with spectroscopic [HF84, FHC86, HF94, CHP94], laser scattering [MFH92] and electric probe [ZH94] arc temperature measurements. For such

Year	Ref.	Remarks	Arc configurations
1977	[Liu77]	1st numerical TIG arc model	180-500A, Ar & N_2
1980	[Fin80]	1st numerical plasma arc model	
1981	[CP81]	1st 2-T plasma arc model	200A transferred plasma arc
1982	[HEP83]	1-T model + T-measurement	100, 200 & 300A, 10 & 20mm, Ar
	[Hsu82]	TIG arc modelling PhD-thesis	see also [HEP83, HP83b, HP84]
1983	[HP83b]	2-T model	10mm 200A Ar
1984	[HP84]	1-T model at elevated press.	5mm, 100 & 200A Ar at 0.1...1.0 MPa
1985	[KL85]	1-T model, flat cathode	5mm, 100 & 200A Ar
	[MS86]	1-T model, flat cathode	6.3 & 10mm, 100 & 200A Ar
1986	[KC86]	1-T model, gas flow effects	5mm, 100 & 200A (also 2mm), Ar
	[FHC86]	Spectrosc. arc T-measurement	5mm, 200A, Ar, steel anode
	[FUM86]	1-T model + cath. shape effect	3mm, 150, 200, 250 & 300A, Ar
	[DC86]	Spectrosc., LTE deviations	4mm, 35A, Ar
1989	[TK90]	1-T model with BFC-numerics	
1990	[DS90]	1-T model with cath. sheath	10mm, 200A, Ar
	[ZDE90]	1-T model + Cu evaporation	10mm, 150A, Ar
	[CSW90]	1-T model + anode depress.	6.3mm, 200A, Ar
1991	[CSW92]	1-T model, 1st param. study	(1.5mm, 50A) ... (6.3mm 300A)
	[WS91]	nontransferred plasma arc model	250, 500 & 750A, Ar
1992	[CS92]	1-T model + weld-pool + evap.	2mm, 100A, Ar
	[ZLM92]	1-T model + cathode sheath	5mm, 200A, Ar
	[LKS92]	1-T model, radiation effects	5mm, 200A, Ar
	[MFH92]	Laser scatt. T-measurement	5mm, 100A, Ar
1993	[ZL93]	Cathode melting effects	100A, Ar
	[GG93]	1-T model + Fe evaporation	10mm, 200 & 300A, Ar
	[Tho93]	Spectrosc. exp., LTE !?	5mm, 100A, Ar
	[Sch93]	1-T model at elevated press.	3mm, 100A, Ar at 1, 5 & 10 MPa
1994	[ZH94]	Exp. Ar-He arc investigation	5 & 10mm, 100A, Ar+He
	[HF94]	Exp. cathode shape effects	5mm, 200A Ar
1995	[ZLMH95]	1-T model + cath. + anode	5mm, 200A Ar, Cu anode

Table 2: Published TIG arc modelling results from 1977 to 1995.

measurements, a *standard arc configuration* was recently proposed (figure 16), which may be also usefull for the (future) production of compareable modelling results.

4.1 Pure argon arc column

The first step in arc modelling was to develop models of the column, which – for specific boundary conditions – deliver arc temperature distributions close to the measured ones. After Liu's first results [Liu77], the arc column model of Hsu for atmospheric [Hsu82, HEP83] as well as for elevated pressure [HP84] argon arcs, showed remarkable agreement with column temperature measurements, provided that the boundary conditions are correctly adjusted. Assuming a flat cathode, these results where confirmed by other authors [KL85, MS86], one of them demonstrating the (negligible) effect of gas flow on TIG arc behaviour to the welding community [KC86]. Similar results where also produced with refined numerical methods [TK90].

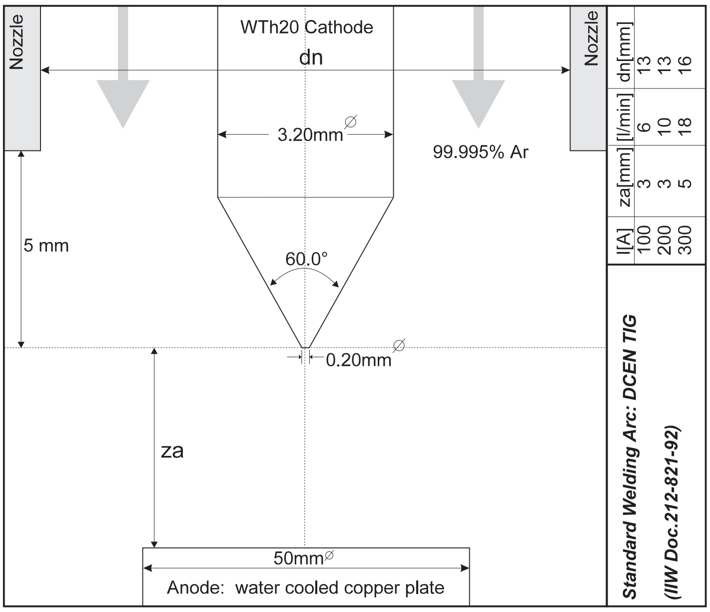

Figure 16: Definition of the *standard TIG arc* configuration [Lan92].

I[A]	1.5mm	2mm	6.3mm	10mm
50	0.652	0.412		
100	1.05	0.748	0.213	
150	1.50	1.11		
200			0.631	0.78...0.83
300			1.05	1.5...2.0

Table 3: Maximum anode heat fluxes (in 10^8 W/m^2) derived from arc modelling, for different arc currents and arc lengths; after [CSW92] (flat cathodes) and [GG93] (10mm arcs with and without iron vapor effects).

For welding applications, the energy density supplied to the anode is of major interest, thus currently available results are given in table 3. The energy densities of $0.2 \ldots 1.5 \cdot 10^8$W/m^2 are consistent with heat input measurements, e.g. those of Nestor [Nes62].
Another important result is the anodic excess pressure from the arc, which may depress the weld pool surface. The results shown in table 4 are consistent for similar models, while the more sophisticated arc model recently developed, shows significantly higher excess pressure values for the 200A 5mm argon arc.

4.2 Two temperature argon arc column modelling

Argon arc columns are usually decribed by a single temperature model, which needs to be extended in column regions, where electron temperature is higher than the heavy particles (gas) temperature. Such effects where first studied for the wall stabilized column of a transferred plasma arc [CP81] and later extended to the free burning arc [HP83b]. Especially in the arc fringes and near the anode, such two temperature models show better agreement with experiment than the 1-T model. As a conclusion, one may state such

I[A]	1.5mm[a]	2mm[a]	3mm[b]	5mm[d]	6.3mm[a]	10mm[c]	20mm[c]
50	58	52					
100	172	168			105	72	38
150	328	333	350				
200			680	1600	519	394	188
250			1100				
300			1700		1048	869	475

Table 4: Published maximum anode surface excess pressure in Pa derived from arc modelling for different arc currents and arc lengths (after [CSW92][a], [FUM86][b], [HEP83][c] and [ZLM92][d]).

models are needed for accurate decription of all arc regions below 9000K (which means the main part of the arc for currents of below 50A and a negligible part for currents above 300A). Another application area may be the computation of helium arcs, a task actually not undertaken.

4.3 Argon arc columns with an evaporating anode

A number of arc applications incorporate evaporating anodes. The influence of metal vapor on arc column behaviour was studied for copper-argon [ZDE90] and iron-argon arcs [GG93]. The effect of metal vapor was modelled by computing the transport coefficients for the corresponding mixtures and taking the transport of the vapor into account. The most important effects are increased arc radiation and significantly higher current densities within the vapor affected anode regions of the column plasma. Thus, the energy density is also affected by anodic evaporation. Naturally, evaporating cathodes give much larger effects.

4.4 Integrated column-electrode modelling

Modelling the arc column only, may not be stated as a model of the arc itself, because some major effects are not computed, but rather used as input boundary conditions. Especially at the cathode, accurate current density and temperature boundary conditions are needed. Thus a model of the nonequilibrium cathode layer [LMZ+93] was integrated into the computation of the arc column [DS90, ZLM92] and used to study cathode melting [ZL93]. Recently, the same model was used to integrate column calculations, boundary layer calculations and heat conduction within the electrodes [ZLMH95]. As can be seen from figure 17, this may be regarded as the first computation of the overall *arc system*. Computed cathode surface temperatures may be compared with measurements recently published [HF92].

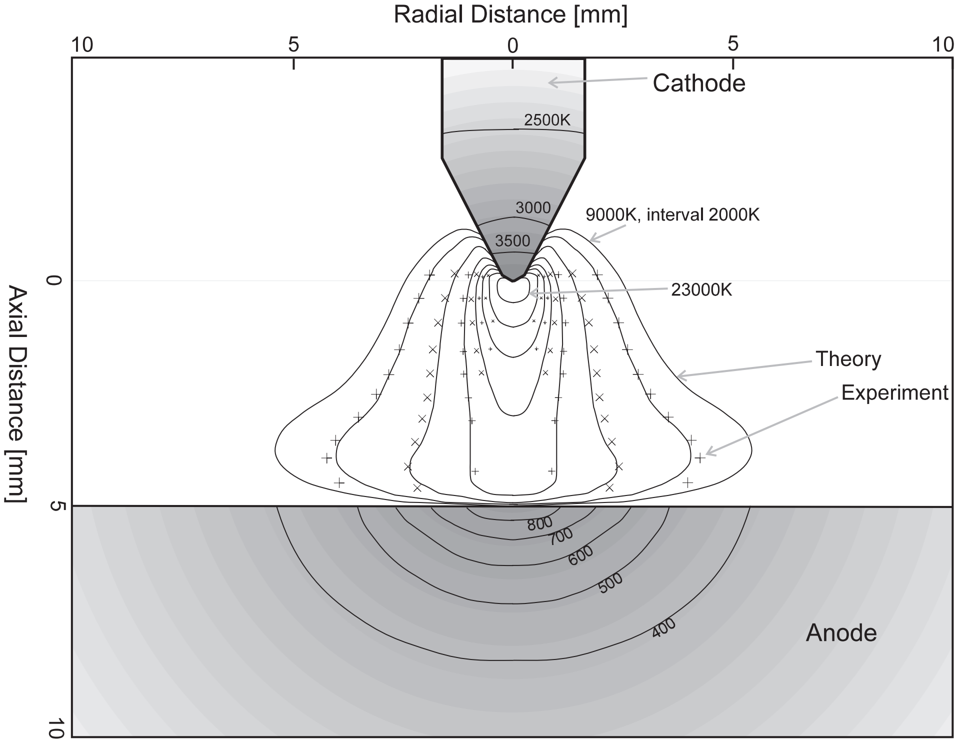

Figure 17: Predicted temperature contours after [ZLMH95], for a 200A arc in argon at 0.1 MPa. The arc system has a 60^o conical cathode of thoriated tungsten of 3.2mm diameter and a copper anode of 5mm thickness. Experimental values [HF84] are shown as points.

5 Plasma arc modelling results

For the plasma arc, the column is constricted by a metallic nozzle, and thus additionally turbulence and swirl effects have to be considered (section 2.3). Principally, one has to distinguish between transferred and nontransferred plasma arc configurations (figure 8).

5.1 Nontransferred plasma arc modelling

A comprehensive laminar treatment of a nontransferred plasma arc was given by Westhoff et.al. [WS91]. Including the effect of swirl into the two dimensional model, the behaviour of the arc plasma inside the torch, as well as the plume formation was predicted. There was sufficient agreement with experimental data, which naturally is available only for the plume region. This work can be regarded as an important progress in predicting torch behaviour almost entirely from first principles.
The recent paper of Murphy et.al. [MK93] presents turbulent modelling results of a *non-transferred* plasma arc (configuration as shown in figure 8). The equations summarized in 2.3, where solved including mixing effects and swirl ($v_\theta \neq 0$). As shown in figure 18, the turbulence effects are quite important and there is sufficient aggreement with temperature measurements (figure 19). At higher current levels the increase in pressure above ambient pressure has to be included into the computations of the transport coefficients. Additionally, Mach-number increases and thus viscous dissipation may become important.

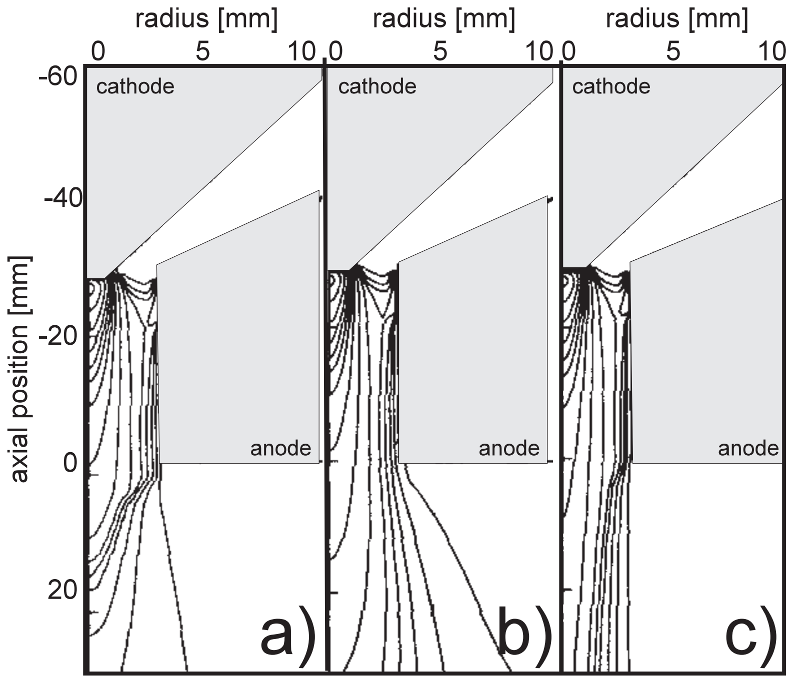

Figure 18: Temperature contours for a plasma torch operating in argon with $I = 400$A and $F = 40$l/min, discharging into (a) an air environment, with turbulent effects considered, (b) an argon environment, with turbulence effects considered, and (c) an air environment, neglecting turbulence effects. The contour steps are $\Delta T = 2000$K; the outermost contour is $T = 1000$K and the innermost is $T = 29000$K (after [MK93]).

While the electrode boundary layers are actually not inluded into such models, the determination of the anode root may be undertaken by applying Steenbecks minimum principle [PHHP93].

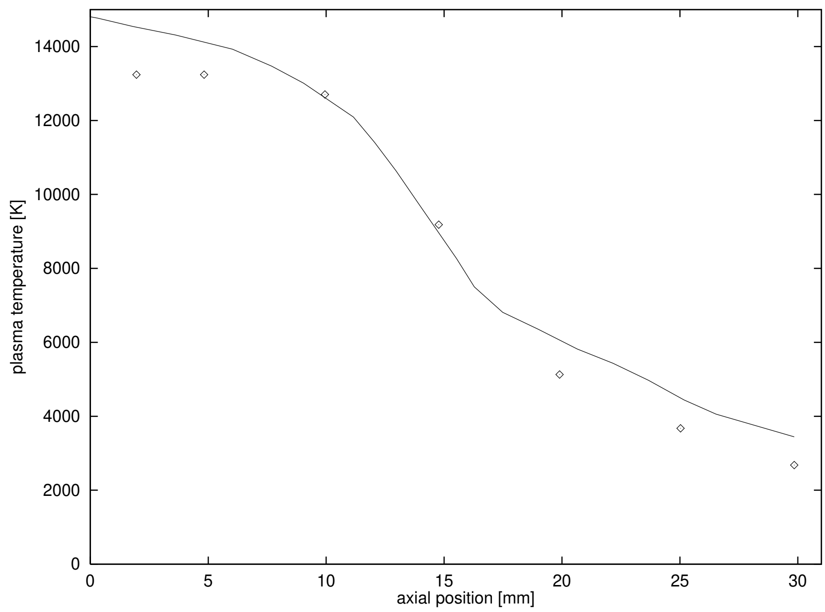

Figure 19: Measured and calculated temperatures along the axis of a non transferred plasma arc (configuration as shown in figure 8, $I = 400A, F = 40$l/min; after [MK93]).

5.2 Transferred plasma arc modelling

First laminar flow modelling of the cathode region of a transferred plasma arc was undertaken in 1980 [Fin80]. After initial laminar computations (275A, 2.73cm and 280A, 5.06cm arc length; [DS90]), turbulent transferred plasma arcs (configuration as stated in figure 8) were recently modeled on an industrial level (see [CDR$^+$93] and figure 20). Agreement with experiment is reasonable for smaller gas flow rates, while higher gas flow rates show some significant discrepancies compared to measured arc temperatures, as shown in figure 21. Additionally numerical problems may occur.

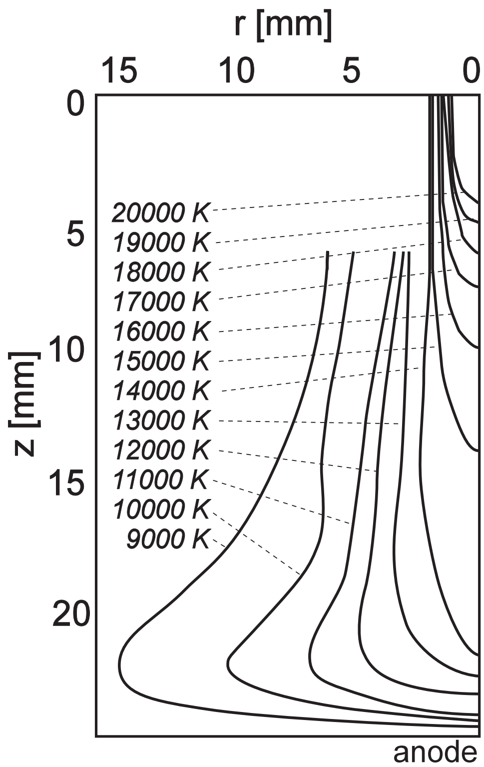

Figure 20: Computed plasma temperature contours (same arc configuration as in figure 21).

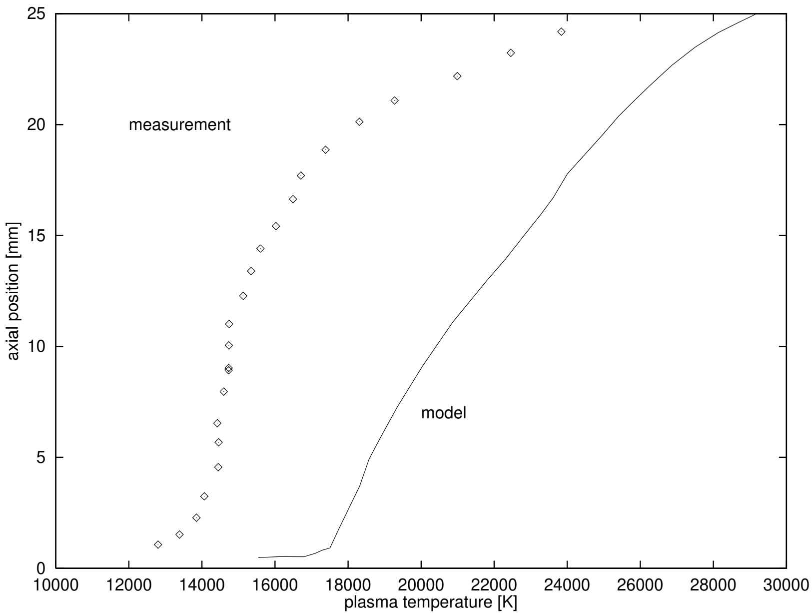

Figure 21: Axial plasma temperature for a transferred plasma arc (cathode tip angle 40^o, $I = 290$A, $m^o_{Ar} = 60$slm, arc length 26mm; after [CDR$^+$93]).

6 Summary and conclusion

6.1 The actual state-of-the-art

There is a remarkable number of results available, which may be regarded as arc column, as well as arc system models. All of them deal with argon arcs at current levels between 50 and several hundred amperes and arc lenghts of about 5mm and above. The modelled arcs are usually longer than the 0.5mm arcs used for high speed welding applications and the development of advanced welding processes [DWW95]. Except for the integrated model [ZLMH95, ZLM92, LKS92], parameter studies may be questionable, because of the cathode and anode boundary conditions needed.
The consistency with experimental arc temperature measurement is obvious, especially if cathode shape effects recently investigated [HF94], can be modelled.
Laminar arc column modelling may be regarded as state of the art in several countries, turbulent plasma arc modelling has recently seen significant progress.
An arc column model *looks like an arc*, but it is not a mathematical representation of the arc itself: The nonequilibrium regions near the electrodes play a major role by forming the solid-plasma interface, thus sustaining the arc's thermal plasma. A model of this boundary layer was presented, but is acually not integrated into an arc system model. Other cathode models are, but did not include the temperature split effect and the space charge sheath potential drop, which was found to be responsible for a major part of both, cathode and anode fall voltage.

6.2 Scientific outlook

For welding applications, there are a number of important research tasks, in order to perform TIG and plasma arc parameter studies and optimizations by numerical modelling. First, one may need a column model including both, temperature split (2-T-model) and the effects of metal vapor. Secondly, a self consistent model of the anode boundary layer is needed, including evaporation. Together with the cathode layer model, this anode layer code has to be integrated into the column simulation. This will probably allow accurate computation of the overall arc voltage, as well as of the anodic heat flow distribution.
For welding speeds above 0.5m/min, three dimensional models may be needed. These are currently not available – maybe because of the changes in the numerical concepts needed, maybe due to non scientific reasons.
Another important area for the application of arc models may lie in the field of visualization, i.e. to explain arc behaviour with the help of the detailed physical data coming from the model.

6.3 Industrial application of arc modelling

For the TIG arc, modelling codes can be developed for industrial applications. These may be used on current low cost workstations and should allow electrode shape, torch and gas optimizations. The anode surface energy density and/or arc pressure distribution may serve as an optimization target. The codes should also deliver input data for the optimization of the overall TIG welding procedure, e.g. for advanced weld pool modelling [ZD93].

The industrial task of plasma torch development will be an important application area of modelling codes in the near future. This may slightly reduce the number of experiments needed, while a *computer aided torch development* requires arc models including turbulence and electrode layer effects. This may be regarded as a task, which is out of the scope of current public research projects.

Acknowledgement

We would like to thank all the authors within the reference list, for their presentation of results from a field characterized by high complexity and – compared to its industrial importance – lack in research funding. We excuse our *welder's viewpoint* and appreciate any comments.

References

[ADDG92] J D Anderson, G Degrez, E Dick, and R Grundmann. *Computational Fluid Dynamics.* Springer-Verlag, 1992.

[Aht65] W F Ahtye. A critical evaluation of methods for calculating transport coefficients for partially and fully ionized gases. Technical Report TN D-2611, NASA, Washington, D.C., Ames Research Center, Moffet Field, California, 1965.

[AIA91] K Adashi, T Inaba, and T Amakawa. Voltage of wall-stabilized argon arc injected with iron powder. In *Xth International Symposium on Plasma Chemistry (ISPC 91)*, page 1.3.10, 1991.

[And90] A Anders. *A Formulary for Plasma Physics.* Akademie-Verlag, 1990.

[Bal88] R Balescu. *Transport Processes in Plasmas*, volume 1 of *Classical Transport Processes.* North-Holland, 1988.

[Ben93] D A Benoy. *Modelling of thermal argon plasmas.* PhD thesis, Dept. of Physics, Univ. of Eindhooven, 1993.

[BH54] W Bez and K H Höcker. Theorie des Anodenfalls. *Z. Naturforsch.*, 9a:72–81, 1954.

[BH55] W Bez and K H Höcker. Theorie des Anodenfalls III. Äquipotentialflächen vor der Lichtbogenanode. *Z. Naturforsch.*, 10a:714–717, 1955.

[BH56a] W Bez and K H Höcker. Theorie des Anodenfalls IV. Der Anodenfall des Homogenkohle-Hochstrombogens in Luft. *Z. Naturforsch.*, 11a:118–123, 1956.

[BH56b] W Bez and K H Höcker. Theorie des Anodenfalls V. Das Zischen des Homogenkohle-Hochstrombogens in Luft. *Z. Naturforsch.*, 11a:192–196, 1956.

[Boh49] D Bohm. Minimum ionic kinetic energy for a stable sheath. In A Guthrie and R K Wakerling, editors, *The characteristics of electrical discharges in magnetic fields*, chapter 3, pages 77–86. McGraw-Hill, 1949.

[BPF54] G Busz-Peuckert and W Finkelnburg. Zum Anodenmechanismus des thermischen Argonbogens. *Z. Phys.*, 144:244–251, 1954.

[BPF55] G Busz-Peuckert and W Finkelnburg. Die Abhängigkeit des Anodenfalles von Stromstärke und Bogenlänge bei Hochtemperaturbögen. *Z. Phys.*, 140:540–546, 1955.

[Bra84] A Brandt. *Multigrid Techniques: 1984 guide with application to fluid dynamics*, volume 85 of *GMD-Studien*. 1984.

[BSL60] R B Bird, W E Stewart, and E N Lightfoot. *Transport Phenomena*. Wiley, 1960.

[CDR+93] J F Coudert, C Delalondre, P Roumilhac, O Simonin, and P Fauchais. Modeling and experimental study of a transferred arc stabilized with argon and flowing in a controlled-atmosphere chamber filled with argon at atmospheric pressure. *Plasma Chem. Plasma Process.*, 13(3):399–432, 1993.

[CG77] N Collings and A E Guile. Continuous anode mode for high-speed tungsten inert gas arc welding. *Proc. IEE*, 124(10):905–908, 1977.

[CHP94] W L Chen, J Heberlein, and E Pfender. Diagnostics of a thermal plasma jet by optical emission spectroscopy and enthalpy probe measurements. *Plasma Chem. Plasma Process.*, 14(3):317–32, 1994.

[CP80] D M Chen and E Pfender. Modeling of the anode contraction region of high intensity arcs. *IEEE Tr. Plasma Sc.*, PS-8(3):252–259, 1980.

[CP81] D M Chen and E Pfender. Two-temperature modeling of the anode contraction region of high-intensity arcs. *IEEE Tr. Plasma Sc.*, PS-9(4):265–274, 1981.

[CS71] T F Chase and W F Savage. Effect of anode composition on tungsten arc characteristics. *Welding Research Supplement*, (11):467, 1971.

[CS92] R T C Choo and J Szekely. Vaporization kinetics and surface temperature in a mutually coupled spot gas tungsten arc weld and weld pool. *Welding J.*, 71(3):77s–93s, 1992.

[CSW90] R R T C Choo, J Szekely, and R C Westhoff. Modeling of high-current arcs with emphasis on free surface phenomena in the weld pool. *Welding J.*, 69(9):346s–361s, 1990.

[CSW92] R T C Choo, J Szekely, and R C Westhoff. On the calculation of the free surface temperature of gas-tungsten-arc weld pools from first principles: Part I. modeling the welding arc. *Metallurgical Tr. B*, 23(3):357–369, 1992.

[DC86] D Degout and A Catherinot. Spectoscopic analysis of the plasma created by a double-flux tungsten inert gas (TIG) arc plasma torch. *J. Phys. D: Appl. Phys.*, 19:811–823, 1986.

[DE90] G J Dunn and T W Eagar. Calculation of electrical and thermal conductivities of metallurgical plasmas. *WRC-Bull.*, H.357:1–21, 1990.

[Den62] F Dennery. Electric field distribution in welding arcs. In *Weld. Inst. Conf. "Physics of the Welding Arc Symposium"*, pages 35–40, 1962.

[Dev67a] R S Devoto. Simplified expressions for the transport properties of ionized monatomic gases. *Phys. Fluids*, 10(10):2105–2112, 1967.

[Dev67b] R S Devoto. Transport coefficients of partially ionized argon. *Phys. Fluids*, 10(2):354–364, 1967.

[DF65] H W Drawin and P Felenbok. *Data for Plasmas in local thermodynamic equilibrium.* Gauthier-Villars, 1965.

[DP80] H A Dinulescu and E Pfender. Analysis of the anode boundary layer of high intensity arcs. *J. Appl. Phys.*, 51:3149–3157, 1980.

[DS90] C Delalondre and O Simonin. Modelling of high intensity arcs including a non-equilibrium description of the cathode sheath. *J. Physique Coll.*, 51(C5):199–206, 1990.

[DWW95] I Decker, J Wendelstorf, and H Wohlfahrt. Laserstrahl-WIG-Schweißen von Aluminiumlegierungen. In *Große Schweißtechnische Tagung, Dresden*, volume 170 of *DVS Berichte*, pages 96–99. DVS, Düsseldorf, 1995.

[Eck61] G Ecker. Electrode components of the arc discharge. *Erg. d. exakt. Naturwissenschaften*, 33:1–104, 1961.

[EPB90] A Essoltani, P Proulx, and M I Boulos. Radiation and self-absorption in argon-iron plasmas at atmospheric pressure. *J. Analytical Atomic Spectroscopy*, 5(9):543–547, 1990.

[ET67] D L Evans and R S Tankin. Measurement of emission and absorption of radiation by an argon plasma. *Phys. Fluids*, 10(6):1137–1144, 1967.

[FHC86] J D A Farmer, G N Haddad, and L E Cram. Temperature determinations in a free-burning arc: III. measurements with molten anodes. *J. Phys. D: Appl. Phys.*, 19:1723–1730, 1986.

[Fin80] J E Fink. Theory and computation of the characteristics of the thermal electric plasma arc for chemical engineering applications. *Chem. Eng. Comm*, 5:37–53, 1980.

[FUM86] D Fan, M Ushio, and F Matsuda. Numerical computation of arc pressure distribution. *Tr. JWRI*, 15:1–15, 1986.

[GG93] J J Gonzalez and A Gleizes. Mathematical modelling of a free burning arc in the presence of metal of vapour. *J. Appl. Phys.*, 74(5):3065–3070, 1993.

[Gli80] S S Glickstein. Arc modelling for welding analysis. In *Arc Physics and Weld Pool Behaviour, London, UK, 8-10 May 1980*, pages 1–16. Abington, UK: Welding Inst., 1980.

[GRH+79] H W Ghent, D W Roberts, C E Hermance, H W Kerr, and A B Strong. Arc efficiencies in TIG welds. In *Arc Physics and Weld Pool Behaviour, Welding Inst., London*, pages 17–23, 1979.

[Gui71] A E Guile. Arc electrode phenomena. *Proc. IEE*, 118(9R):1131–1154, 1971.

[Gui84] A E Guile. Electric arcs: their electrode processes and engineering applications. *IEE Proc. A*, 131(7):450–480, 1984.

[Hac85] W Hackbusch. *Multi-grid methods and applications*. Springer, 1985.

[Han70] K Hanjalic. *Two dimensional asymmetric flow in ducts*. PhD thesis, Imperial College, University of London, 1970.

[HB55] K H Höcker and W Bez. Theorie des Anodenfalls II. Möglichkeiten und Grenzen der Feldionisierung. *Z. Naturforsch.*, 10a:706–714, 1955.

[HCB64] J O Hirschfelder, C F Curtis, and R B Bird. *Molecular Theory of Gases and Liquids.* John Wiley, 2nd edition, 1964.

[HEP83] K C Hsu, K Etemadi, and E Pfender. Study of the free-burning high-intensity argon arc. *J. Appl. Phys.*, 54:1293–1301, 1983.

[HF84] G N Haddad and A D J Farmer. Temperature determination in a free burning arc: I. experimental techniques and results in argon. *J. Phys. D: Appl. Phys.*, 17:1189–1196, 1984.

[HF92] J Haidar and A J D Farmer. A method for the measurement of the cathode surface temperature for a high current free-burning arc. *Rev. Sci. Instrum.*, 64(2):542–547, 1992.

[HF94] J Haidar and A J D Farmer. Large effect of cathode shape on plasma temperature in high-current free-burning arcs. *J. Phys. D: Appl. Phys.*, 27(3):555–560, 1994.

[HFKC86] G N Haddad, A J D Farmer, P Kovitya, and L E Cram. Physical processes in gas-tungsten arcs. *IEEE Tr. Plasma Sci.*, PS14(4):333–336, 1986.

[HL67] M I Hoffert and H Lien. Quasi-one-dimensional, non-equilibrium gas dynamics of partially ionized two-temperature argon. *Phys. Fluids*, 10(8):1769–1777, 1967.

[HM94] R Hajossy and I Morva. Cathode and anode falls of arcs with fusible electrodes. *J. Phys. D: Appl. Phys.*, 27:2095–2101, 1994.

[HP83a] K C Hsu and E Pfender. Analysis of the cathode region of a free-burning high intensity argon arc. *J. Appl. Phys.*, 54(7):3818–3824, 1983.

[HP83b] K C Hsu and E Pfender. Two-temperature modeling of the free-burning, high-intensity arc. *J. Appl. Phys.*, 54:4359–4366, 1983.

[HP84] K C Hsu and E Pfender. Modeling of a free-burning, high-intensity arc at elevated pressures. *Plasma Chem. Plasma Process.*, 4(3):219–234, 1984.

[Hsu82] K C Hsu. *A self consistent model for the high intensity free burning argon arc.* PhD thesis, Univ. of Minnesota, Minneapolis, USA, 1982.

[IIOY94] K Ishizaki, K Ishii, T Okada, and S Yokoya. Anode phenomena and penetration in He-TIG arc welding. *Welding International*, 8(8):593–598, 1994.

[JSCQ94] P G Jönsson, J Szekely, R T C Choo, and T P Quinn. Mathematical models of transport phenomena associated with arc welding process: a survey. *Modelling Simul. Mater. Sci. Eng.*, 2:995–1016, 1994.

[KB77] D Kannappan and T K Bose. Transport properties of a two temperature argon plasma. *Phys. Fluids*, 20(10):1668–1673, 1977.

[KC86] P Kovitya and L E Cram. A two-dimensional model of gas tungsten welding arcs. *Welding J.*, (12):34s–39s, 1986.

[KL85] P Kovitya and J J Lowke. Two-dimensional analysis of free burning arcs in argon. *J. Phys. D: Appl. Phys.*, 18:53–70, 1985.

[Kru70] C H Kruger. Nonequilibrium in confined arc plasmas. *Phys. Fluids*, 13(7):1737–1746, 1970.

[Lan92] J F Lancaster. TIG arc configuration for temperature and other measurements. IIW Doc. No. 212-821-92, 1992.

[Liu77] C H Liu. *Numerical analysis of the anode region of high intensity arcs.* PhD thesis, Dept. of Mech. Eng. , University of Minnesota, Minneapolis, USA, 1977.

[LKS92] J J Lowke, P Kovitya, and H P Schmidt. Theory of free-burning arc columns including the influence of the cathode. *J. Phys. D: Appl. Phys.*, 25(11):1600–1606, 1992.

[LMZ+93] J J Lowke, R Morrow, P Zhu, J Haidar, and A J D Farmer. A one-dimensional theory for the electrode sheaths of electric arcs. *J. Phys. D: Appl. Phys.*, 26:634–642, 1993.

[LOS92] V M Lelevkin, D K Otorbaev, and D C Schram. *Physics of Non-Equilibrium Plasmas.* North-Holland, 1992.

[LS72] B E Launder and D B Spalding. *Mathematical Models of Turbulence.* Academic Press, 1972.

[LS74a] B E Launder and B I Sharma. Application of the energy dissipation model of turbulence to the calculation of flow near a spinnng disk. *Lett. Heat Mass Transfer*, 1:131–138, 1974.

[LS74b] B E Launder and D B Spalding. The numerical computation of turbulent flows. *Computer Methods in Applied Mechanics and Engineering*, 3:269–289, 1974.

[MA69] R C Miller and R J Ayen. Temperature profiles and energy balances for an inductively coupled plasma torch. *J. Appl. Phys.*, 40(13):5260–5273, 1969.

[MF57] H Maecker and W Finkelnburg. Elektrische Bögen und thermisches Plasma. In S Flügge, editor, *Handbuch der Physik*, volume 22, pages 254–444. Springer, 1957.

[MFH92] A B Murphy, A J D Farmer, and J Haidar. Laser-scattering measurement of temperature profiles of a free-burning arc. *Appl. Phys. Lett.*, 60(11):1304–1306, 1992.

[MK93] A B Murphy and P Kovitya. Mathematical model and laser-scattering temperature measurements of a direct-current plasma torch discharging into air. *J. Appl. Phys.*, 73(10):4759–4769, 1993.

[MM73] G Mondain-Monval. Physical properties of fluids in welding arc. IIW-Doc. No. 212-264-73, 1973.

[MP94] B Mohammadi and O Pironneau. *Analysis of the K-Epsilon turbulence model.* Research in Applied Mathematics. Masson, John Wiley & Sons, 1994.

[MS86] J McKelliget and J Szekely. Heat transfer and fluid flow in the welding arc. *Metallurgical Tr. A*, 17:1139–1148, 1986.

[Nem94] V A Nemchinsky. Plasma parameters near a small anode in a high pressure arc. *J. Phys. D: Appl. Phys.*, 27:2515–2521, 1994.

[Nes62] O H Nestor. Heat intensity and current density distribution at the anode of high current inert gas arcs. *J. Appl. Phys.*, 33(5):1638–1648, 1962.

[NP77] V A Nemchinsky and L N Peretts. Anode sheath in a high pressure, high current arc. *Sov. Phys. - Tech. Phys.*, 22:1083–1087, 1977.

[NP89] I P Nazarenko and I G Panevin. Analysis of the near-anode processes characters in argon arc discharges of high pressure. *Contr. Plasma Phys.*, 29(3):251–261, 1989.

[PA76] P D Prewett and J E Allen. The double sheath associated with a hot cathode. *Proc. Roy. Soc. Lond.*, A348:435–446, 1976.

[Pan93] R L Panton. Fluid dynamics, equilibrium. In G L Trigg, editor, *Encyclopedia of Applied Physics*, volume 6, pages 409–436. VCH Publishers, 1st edition, 1993.

[Pat80] S V Patankar. *Numerical heat transfer and fluid flow.* Hemisphere Publishing, 1980.

[Pfe78] E Pfender. Electric arcs and arc gas heaters. In M N Hirsh and H J Oskam, editors, *Gaseous Electronics*, volume 1, chapter 5, pages 291–398. Academic Press, 1978.

[Pfe80] E Pfender. Energy transport in thermal plasmas. *Pure & Appl. Chem.*, 52:1773–1800, 1980.

[PHHP93] S Paik, P C Huang, J Heberlein, and E Pfender. Determination of the arc-root position in a dc plasma torch. *Plasma Chem. Plasma Process.*, 13(3):379–397, 1993.

[Pot66] A V Potapov. Chemical equilibrium in multitemperature systems. *High. Temp.*, 4(1):48–51, 1966.

[PS72] S V Patankar and D B Spalding. A calculation procedure for heat, mass and momentum transfer in the three-dimensional parabolic flows. *Int. J. Heat Mass Transfer*, 15:1787–1806, 1972.

[PTV+92] W H Press, S A Teukolsky, W T Vetterling, Flannery, and Brain P. *Numerical Recipes in C.* Cambridge University Press, 2nd edition, 1992.

[Ret94] B Rethfeld. Modellierung der katodennahen Plasmarandschicht einer Lichtbogenentladung. Master's thesis, Inst. f. Theoretische Physik, TU-Braunschweig, Germany, 1994.

[Rie91] K U Riemann. The bohm criterion and sheath formation. *J. Phys. D: Appl. Phys.*, 24:493–518, 1991.

[RKT+95] B Rethfeld, T Klein, C Tix, J Wendelstorf, and G Simon. Modellierung der katodennahen Plasmarandschichten eines WIG-Lichtbogens. *Verh. d. DPG*, (VI) 30:P 19.46, S.243, 1995.

[Rod72] W Rodi. *The predictions of free turbulent boundary layers by use of a two equation model of turbulence.* PhD thesis, Imperial College, University of London, 1972.

[RS71] R Reeves-Saunders. Observation of a transition into a stable mode for an arc burning on a rotating anode. *J. Phys. D: Appl. Phys.*, 4:L25–L28, 1971.

[RWKS96] B Rethfeld, J Wendelstorf, T Klein, and G Simon. A self–consistent model for the cathode fall region of an electric arc. *J. Phys. D: Appl. Phys.*, 29:121–128, 1996.

[Sch24] W Schottky. Diffusionstheorie der positiven Säule. *Physik Z.*, 25:635–640, 1924.

[Sch63] P A Schoeck. An investigation of the anode energy balance of high intensity arcs in argon. In W Ibele, editor, *Modern Developments in Heat Transfer*, pages 353–400. Academic Press, 1963.

[Sch93] H P Schmidt. Investigation of the high pressure argon arc. In G Ecker, U Arendt, and J Böseler, editors, *XXI. International Conference on Phenomena in Ionized Gases (ICPIG)*, volume II, pages 72–74. APP Ruhr Universität Bochum, 1993.

[SEHP82] N A Sanders, K Etemadi, K C Hsu, and E Pfender. Studies of the anode region of the high intensity argon arc. *J. Appl. Phys.*, 53(6):4136–4145, 1982.

[SP84] N A Sanders and E Pfender. Measurement of anode falls and anode heat transfer in atmospheric pressure high intensity arcs. *J. Appl. Phys.*, 55(3):714–722, 1984.

[Tho93] M F Thornton. Spectroscopic determination of temperature distributions for a TIG arc. *J. Phys. D: Appl. Phys.*, 26:1432–1438, 1993.

[TK90] M C Tsai and S Kou. Heat transfer and fluid flow in welding arcs produced by sharpened and flat electrodes. *Int. J. Heat Mass Transfer*, 33(10):2089–2098, 1990.

[UFT94] M Ushio, D Fan, and M Tanaka. A method of estimating the space-charge voltage drop for thermionic arc cathodes. *J. Phys. D: Appl. Phys.*, 27(3):561–566, 1994.

[Vil82] F Vilsmeier. *Laserstreuung und Stromtransport im Argon-Bogenplasma.* PhD thesis, TU München, Germany, 1982.

[Wes89] R C Westhoff. Master's thesis, MIT, Boston, USA, 1989.

[WS91] R Westhoff and J Szekely. A model of fluid heat flow, and electromagnetic phenomena in a nontransferred arc plasma torch. *J. Appl. Phys.*, 70(10):3455–3466, 1991.

[YA77] T Yoshida and K Akashi. Particle heating in a radio frequency plasma torch. *J. Appl. Phys.*, 48(6):2252–2260, 1977.

[ZD93] T Zacharia and S A David. Heat and fluid flow in welding. In H Cerjak and K Easterling, editors, *Mathematical Modelling of Weld Phenomena*, volume I, pages 3–23. Institute of Materials, 1993.

[ZDE90] G Y Zhao, M Dassanayake, and K Etemadi. Numerical simulation of a free-burning argon arc with copper evaporation from the anode. *Plasma Chem. Plasma Process.*, 10(1):87–98, 1990.

[ZH94] J Zijp and K Hiraoka. Basic parameters of heat transport in argon-helium mixed gas arcs. *Welding International*, 8(7):518–524, 1994.

[ZHP94] X Zhou, J Heberlein, and E Pfender. Theoretical study of factors influencing arc erosion of cathode. *IEEE Transactions on Components, Packaging, and Manufacturing Technology, Part A*, 17(1):107–112, 1994.

[ZL93] P Zhu and J J Lowke. Theoretical study of the melting of the cathode tip of a free burning arc in argon for various conical angles. *J. Phys. D: Appl. Phys.*, 26:1073–1076, 1993.

[ZLM92] P Zhu, J J Lowke, and R Morrow. A unified theory of free burning arcs, cathode sheaths and cathodes. *J. Phys. D: Appl. Phys.*, 25:1221–1230, 1992.

[ZLMH95] P Zhu, J J Lowke, R Morrow, and J Haidar. Prediction of anode temperatures of free burning arcs. *J. Phys. D: Appl. Phys.*, 28:1369–1376, 1995.

Glossary of symbols

Symbol	Eqn.	Unit	
a			Index for neutral atoms
A_{Rich}	32	$\mathrm{A/(m^2\ K^2)}$	Richardson's constant
C_i	5	1	Particle concentration of species i
c_p	18	J/(kg K)	Specific heat at constant pressure
$D(\ldots)/Dt$			Substantial derivative $\frac{\partial(\ldots)}{\partial t} + \vec{\mathbf{v}} \cdot \vec{\nabla}(\ldots)$
D	10	$\mathrm{m^2/s}$	Diffusion coefficient
D_{ee}	25	$\mathrm{m^2/s}$	Self diffusion coefficient of the electrons
D_e^T		kg s/m	Thermal diffusion coefficient of the electrons
D_{ia}		$\mathrm{m^2/s}$	Diffusion coefficient of ions in neutral atoms
e		C	Index for electrons; elementary charge
E_{ion}		J	Ionization energy
δE	15	J	Lowering of the ionization energy
g_j		1	Partition function of species j
h			Index for the heavy particle gas
h	17	J/kg	plasma enthalpy
i			Index for ions
$\vec{\mathbf{j}}$		$\mathrm{A/m^2}$	Electric current density vector, e.g. $\{j_r, j_z, j_\theta\}$
j_c	32	$\mathrm{A/m^2}$	Current density of emission electrons in the sheath
j_i	34	$\mathrm{A/m^2}$	Current density of ions in the sheath
j_p	35	$\mathrm{A/m^2}$	Current density of plasma electrons in the sheath
j_{Rich}	32	$\mathrm{A/m^2}$	Richardson current density
j_{tot}	36	$\mathrm{A/m^2}$	Total electric current density
Ma		1	Mach number
m_j		kg	Mass of particle j
n		$\mathrm{1/m^3}$	Total number density
$n_{a,\mathrm{LTE}}$	14	$\mathrm{1/m^3}$	Equilibrium density of the neutral atoms
n_j		$\mathrm{1/m^3}$	Number density of species j
$n_{c,SE}$	33	$\mathrm{1/m^3}$	Density of emission electrons at the sheathedge
$n_{e,SE}$		$\mathrm{1/m^3}$	Density of electrons and ions at the sheathedge
$n_{p,SE}$		$\mathrm{1/m^3}$	Density of plasma electrons at the sheathedge
$\dot{n}_e$	22	$\mathrm{1/(m^3 s^1)}$	Electron and ion generation rate
p	17	Pa	Isotropic pressure
$\vec{\mathbf{q}}$		$\mathrm{W/m^2}$	Heat flux vector
q_C	37	$\mathrm{W/m^2}$	Net energy flux density towards the cathode
Q_{jk}		$\mathrm{m^{-2}}$	Cross section for collisions of particles j with particle k
$\tilde{Q}_{\mathrm{Coul}}$	29	$\mathrm{m^2}$	Linear combination of collision integrals for coulomb collisions
$\tilde{Q}_{ea}$	28	$\mathrm{m^2}$	Linear combination of collision integrals for electron–atom collisions
Re		1	Reynold's number $\rho v l/\mu$=inertia force/viscous force
S_R		$\mathrm{W/m^3}$	Plasma radiation emission coefficient
T_e		K	Temperature of the electron gas
$T_{e,SE}$		K	Temperature of the electron gas at the sheathedge
T_h		K	Temperature of the heavy particle gas
T_C		K	Cathode temperature
T_P		K	Plasma temperature in distance d_{tot} from the cathode surface
u_{Bohm}	31	m/s	Bohm velocity
$u_{i,SE}$		m/s	Velocity of the ions at the sheathedge ($= u_{\mathrm{Bohm}}$)

u_j		m/s	Drift velocity of the species j
v_c		m/s	Local speed of sound
v_j^{th}		m/s	Mean thermal velocity of the species j: $\sqrt{\frac{8k_\mathrm{b}T_j}{\pi m_j}}$
$\vec{\mathbf{v}}$		m/s	velocity vector, e.g. $\{v_r, v_z, v_\theta\}$
V		V	Electric potential
V_C		V	Potential at the cathode surface, defined as zero [V]
V_P		V	Potential drop over the distance d_tot from the cathode surface [V]
V_{SE}		V	Potential drop over the sheath (sheathpotential)
W_{eh}	27	W/m^3	Energy exchange per volume unit due to elastic collisions of electrons with heavy particles
α_rec		m^6/s	Recombination coefficient
α_ion		1	Degree of ionization
Γ_j		m^{-2}s^{-1}	Diffusion flux density of species j
λ_Debye	16	m	Debye length
λ_j		W/(m K)	Thermal conductivity of species j
Φ_C		J	Cathode work function
ρ		kg/m^3	Total mass density
σ		S/m	Electrical conductivity
μ		kg/(m s)	Viscosity